Seventh Framework Programme FP7-SPACE-2010-1
Stimulating the development of downstream GMES services

Grant agreement for: Collaborative Project. Small- or medium scale focused research project
Project acronym: **SIDARUS**
Project title: **Sea Ice Downstream services for Arctic and Antarctic Users and Stakeholders**

Grant agreement no. 262922
Start date of project: 01.01.11
Duration: 36 months
Project coordinator: Nansen Environmental and Remote Sensing Center, Bergen, Norway

D5.3: SAR image analyses

Due date of deliverable: 31.12.2012

Actual submission date: 04.03.2013

Organization name of lead contractor for this deliverable: AWI

Project co-funded by the European Commission within the Seventh Framework Programme, Theme 6 SPACE		
Dissemination Level		
PU	Public	X
PP	Restricted to other programme participants (including the Commission)	
RE	Restricted to a group specified by the consortium (including the Commission)	
CO	Confidential, only for members of the consortium (including the Commission)	

ISSUE	DATE	CHANGE RECORDS	AUTHOR
0	24/03/2011	Template	L.H. Pettersson
1.0	19/12/2012	Draft	Dierking et al.
1.1	02/01/2013	Extended Version	Dierking et al.
1.2	11/01/2013	Final Version	Dierking et al.

SIDARUS CONSORTIUM

Participant no.	Participant organisation name	Short name	Country
1 (Coordinator)	Nansen Environmental and Remote Sensing Center	NERSC	NO
2	Alfred-Wegener-Institut für Polar-und Meeresforschung	AWI	DE
3	Collecte Localisation Satellites SA	CLS	FR
4	University of Bremen, Institute of Environmental Physics	UB	DE
5	The Chancellor, Masters and Scholars of the University of Cambridge	UCAM	UK
6	Norwegian Meteorological Institute, Norwegian Ice Service	Met.no	NO
7	Scientific foundation Nansen International Environmental and Remote Sensing Centre	NIERSC	RU
8	B.I. Stepanov Institute of Physics of the National Academy of Sciences of Belarus	IPNASB	BR

Table of Contents

List of Figures

List of Tables

SUMMARY

In this report we present the status of work on the use of SAR images for information retrieval about sea ice conditions and iceberg occurrences. Single sections of the report focus on sea ice classification, iceberg detection and tracking, and sea ice motion and deformation analyses. These tasks were identified as important elements for marine monitoring services.

For sea ice classification, the use of image pairs acquired at HH- and HV-polarization (employing Radarsat-2 ScanSAR dual-polarization mode) was investigated. The improvement in classification of ice types by use of HH- and HV-polarization compared to single polarisation has been investigated. The separation of water and ice is improved when both polarizations are available. A clear advantage of the dual-polarization mode for discriminating different ice types has not been investigated yet, but for the ice-water discrimination an automated algorithm based on Neural Network classification has been implemented for a test site around Svalbard. This ice-water discrimination is presently under validation. On the basis of single-polarization radar images (Envisat ASAR) acquired during winter in the central Arctic, the performance of Bayesian and Neural Network classification was assessed in comparison to ice charts and interpretations of sea-ice mapping specialists. It was found that in many cases multi-year, rough first-year, smooth first-year, and new ice could be distinguished with varying accuracies. The achievable correspondence between the results of the algorithms and the complementary data sets was from 68 to 91% for multi-year ice and from 83 to 99% for first-year ice (including smooth and rough types) in the case of the Neural Network approach, and between 40 and 90% for multi-year ice and from 88 to 99% for first-year ice in case of the Bayesian algorithm.

The second task focussed on improving the detection of smaller icebergs that drift in the open ocean or are trapped in sea ice. For this purpose, Radarsat-2 ScanSAR-Wide (spatial resolution 50 m) and ScanSAR-Narrow (25m) images were analysed. Results are that detections from HV-polarized images are less reliable and that a spatial resolution of 25m increases the rate of reliable detections considerably. To improve the identification of icebergs in sea ice, initial tests with different methods for image segmentation were carried out. The MDL (minimum description length) algorithm is found to be most promising for sea ice segmentation, but a number of problems have still to be solved in practical applications.

For sea ice drift and deformation monitoring, an algorithm was implemented and tested using Envisat single-polarization images from a polynia region in the Weddell Sea (Antarctic) and dual-polarization ScanSAR images from Radarsat-2, acquired over Fram Strait. The algorithm requires stable ice structures that can be identified in two consecutive SAR images. This condition is usually fulfilled in the pack ice with its prominent floes and deformation zones. A procedure was developed to assess the reliability of the retrieved ice drift patterns if no additional buoy data are available. It is found that the drift fields derived from HH- and HV-polarized images differ slightly since the sensitivity to certain ice structures depends on polarization. This item needs to be further addressed.

1 Introduction – Objectives and Contents of the Report

This report is a deliverable for WP-5 of the SIDARUS project, which covers the second project year and is related to Task 5.3 “Implementation of algorithms” and Task 5.4 “Application and testing of the toolbox for producing SAR sea ice and iceberg products”. The initial idea was to interface the different algorithms in the SARTool Software developed by CLS. However, during the course of the work it was decided that it is more efficient to provide individual implementations of the single algorithms, considering the differences in computer environments of the participating groups and potential problems in the integration of needed software modules that have been already available before the SIDARUS-project was started.

A large part of this report focuses on the description of the implemented algorithms and methods as required in Task 5.3. But in addition, we include also the results of first tests using Envisat and Radarsat-2 imagery acquired over different sea ice regions. These activities are related to Task 5.4. The report is divided into three thematic sections:

(1) Sea ice classification (main responsibility NERSC and NIERSC, see section 2)

(2) Iceberg detection and tracking (main responsibility CLS, see section 3)

(3) Monitoring of sea ice drift and deformation (main responsibility AWI, see section 4)

Each section is complemented by figures and graphs which clarify concepts and demonstrate possibilities of visualizing results.

We dedicate this report to our colleague Vitaly Alexandrov, who deceased unexpectedly during the course of this work.

The SIDARUS-team

2 Sea Ice Classification

2.1 Introduction

This section of the report deals with the separation of different ice types in radar images. Two data types are considered: in chapter 2.2 (prepared by NERSC), the potential of dual-polarization image products from Radarsat-2, acquired at like- and cross-polarization, is investigated. To this end, backscattering intensities for different ice types are determined and compared to one another. In chapter 2.3 (prepared by NIERSC), the focus is on single-polarization ENVISAT ASAR images, on which more advanced classification methods are applied.

2.2 Radarsat-2: Dual-Polarization

Mohamed Babiker, NERSC

Sea Ice monitoring and classification relies heavily on synthetic aperture radar (SAR) imagery. These sensors record data either at horizontal polarization (RADARSAT-1) or vertically polarized (ERS-1 and ERS-2). Many algorithms have been developed to discriminate sea ice types and open water using single polarization images. Ice type classification, however, is still ambiguous in some cases. In this study we investigated Radarsat2 SAR signatures of various sea ice types identified in HH and HV ScanSAR Wide (SCW) images. Our goal is the development of classification algorithms to be used in operational sea ice monitoring and research, based on images from Radarsat-2 and from future multi-polarization SAR missions. Table 2-1 shows some technical specification of the Radarsat-2 ScanSAR Wide image.

Table 2-1 Technical specification of the ScanSAR Wide

Beam Mode	ScanSAR Wide (SCW)
Beams	W1 + W2 + W3 + S7
Product	SGF (Path image)
Processing level	Georeferenced
Nominal Pixel Spacing	50 x 50
Resolution	160 – 72.1 x 100
Nominal Scene Size	500 x 500
Range Incident Angle	20 – 49 (20-31, 31-39, 39-45, 45-49)
No Looks	4 x 2
Polarization	HH + HV

2.2.1 Data

Ten images were selected (a list is provided in Table 2-2) covering the Fram Strait (Figure 2.1). The images are covering the period from February to April 2012. All the images are from the descending pass acquired ca the same time (morning time) to reduce variation in backscattering due to other factors.

Table 2-2 list of images used

Date	Time	Beam	Pass	Polarization
23022012	07:50:25	W1W2W30S7	Descending	HH HV
24022012	07:21:00	W1W2W30S7	Descending	HH HV
27022012	07:34:06	W1W2W30S7	Descending	HH HV
50032012	07:29:25	W1W2W30S7	Descending	HH HV
12032012	07:25:13	W1W2W30S7	Descending	HH HV
15032012	07:37:49	W1W2W30S7	Descending	HH HV
22032012	07:33:37	W1W2W30S7	Descending	HH HV
28032012	07:58:49	W1W2W30S7	Descending	HH HV
11042012	07:50:36	W1W2W30S7	Descending	HH HV
18042012	07:46:25	W1W2W30S7	Descending	HH HV

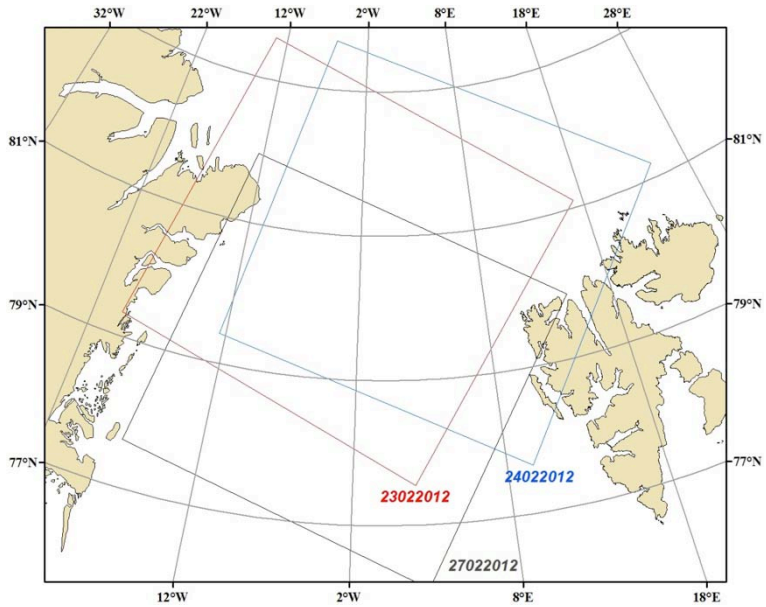

Figure 2-1map of the Fram Strait with frame of the some of the images

2.2.2 Methodology

The "Next ESA SAR Toolbox" (NEST) was used for reading, calibration and normalization of the SAR images. NEST has been developed by Array Systems Computing Inc. of Toronto Canada under ESA Contract number 20698/07/I-LG and can be also used for post-processing, analyzing, and visualizing the large archive of Leve-1 data of the ESA SAR missions. According to the NEST home page (://liferay.array.ca:8080/web/nest/nest-home), it supports ERS1 & 2, ENVISAT, as well as third party SAR-data from JERS SAR, ALOS PALSAR, TerraSAR-X, Radarsat-1&2 and Cosmo-Skymed. NEST is open source and developed under the GNU public license and comes with full source code in Java™. The steps involved in our image processing are:

(1) Reading

The basic file from Radarsat-2 contains one product information file (ascii file in extensible markup language (XML) format), one to four image files (image pixel data; the raster SAR image for a given polarization in Geotiff) and support files (a description of the product contents in HTML, XML; they are not mandatory) (Figure2.2). These files data can be read by several software packages.

(2) Calibration

NEST performs absolute radiometric calibration for Radarsat-2 products by applying the sigma-naught (equation 2.2), beta-naught (equation 2.1) and gamma-naught look-up tables provided with the image product. (Note that all parameters are quantities characterizing the backscattered intensity). The equation for beta-naught reads:

$$ß_J^0 = 10 * \log_{10}[DN_j^2 + A3 / A2_j]\, dB \qquad (2.1)$$

where *DN* is the pixel value, *A2j is the scaling gain value for the jth pixel, and A3 is the fixed offset.* Conversion from beta naught to sigma-naught is carried out using

$$\sigma_j^0 = B_j^0 + 10 * \log_{10}(\sin I_j)\, dB \qquad (2.2)$$

where I_j *is incident angel at the j pixel.*

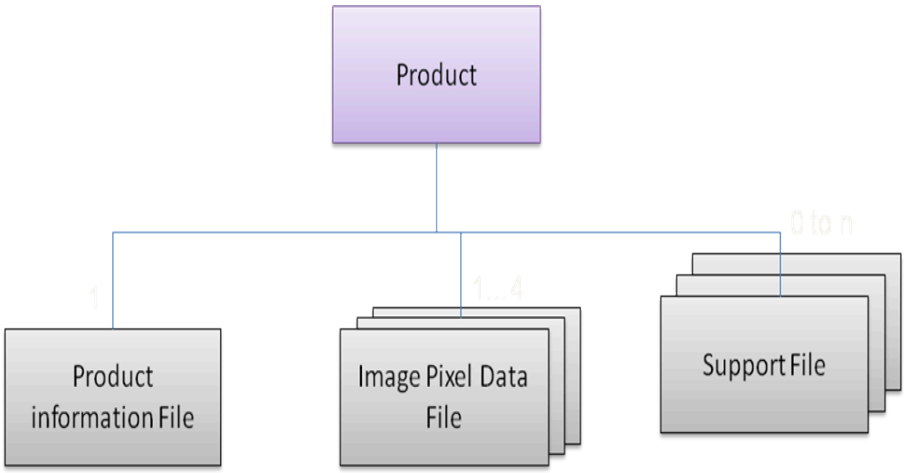

Figure 2-2 Product compositions

(3) Range Normalization

In SAR images the Incident angle varies from near range to far range. The backscattered intensity is decreasing with increasing incidence angle. For image analysis it is of advantage if identical surface types are displayed with the same average gray tone over the full image width. To this end sigma-naught has to be multiplied by a range normalization function. This function depends on the surface type and image polarization. For many ice types, the appropriate function depends on the tangens of the incidence angle to the power of 1.5 for both VV and HH polarization

This formula was originally developed for the SAR Wide Swath ENVISAT images; since there is no common procedure yet for normalizing Radarsat-2 images we are testing this formula on them. After all selected images were calibrated, the normalization formula was applied. In the following, we analyze the images before and after normalization.

(4) Signature Analysis

Sigma-naught values representing the main ice types (first year ice, multiyear ice, and nilas) were extracted by polygons for all images before and after normalization. Then, sigma-naught at HH-polarization was plottet for each ice type against HV polarization to see if there are differences in radar intensity that can help to differentiate between the different ice types. This procedure was applied both before and after normalization. The following graphs (Figures 2.4, 2.5 and 2.6) show these results.

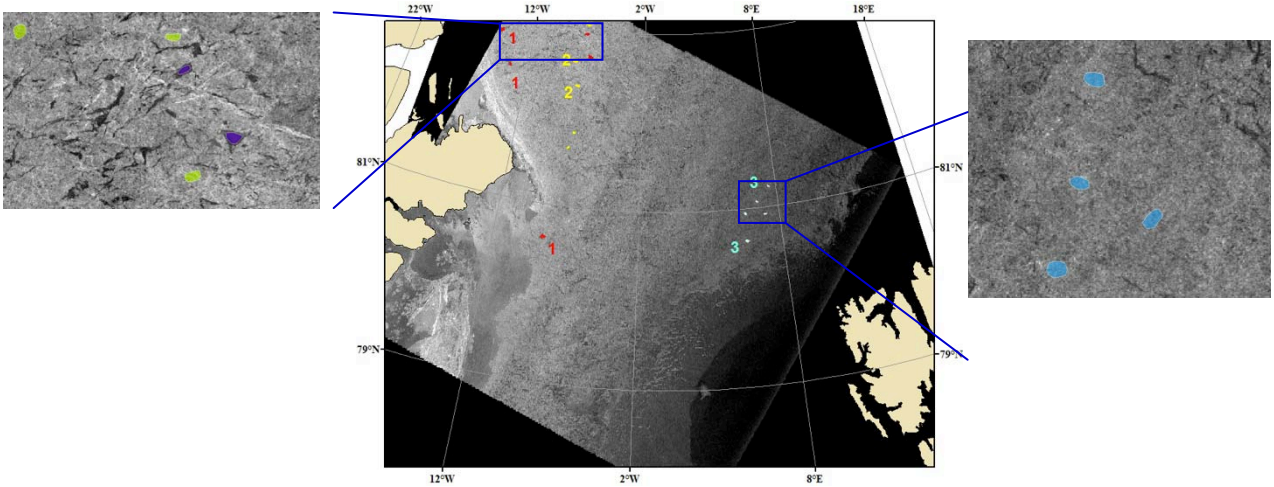

Figure 2-3 Radarsat-2 image of the 23 February 2012 covering Fram Strait. The image shows how sigma-naught was extracted for the different ice types

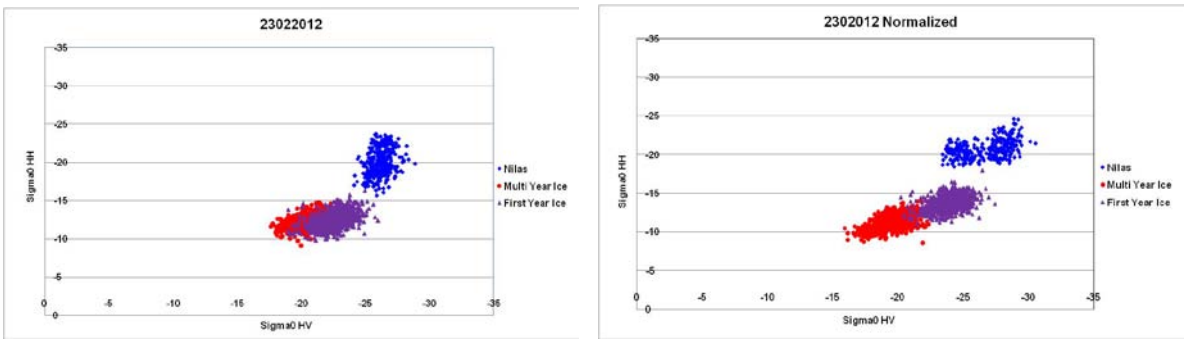

Figure 2-4 Graphs showing sigma-naught values for HH- and HV-polarization extracted from the image of February 23, 2012, (left) before normalization and (right) after normalization

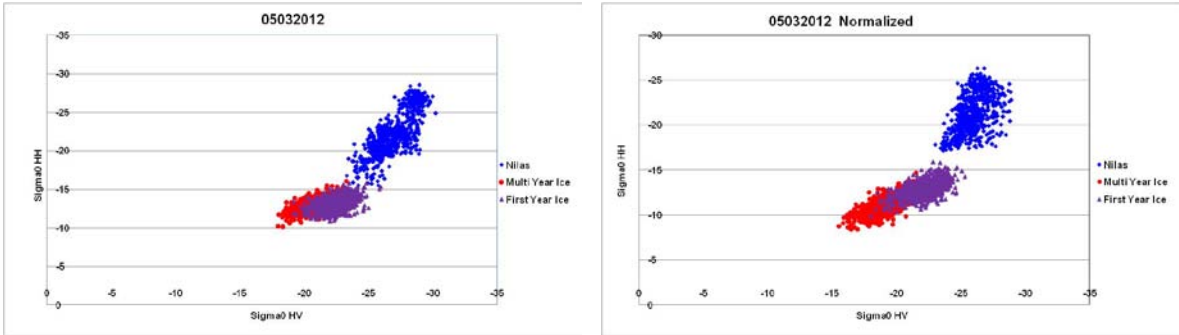

Figure 2-5 Graphs showing sigma-naught values for HH- and HV-polarization extracted from the image of March 5, 2012, (left) before normalization and (right) after normalization

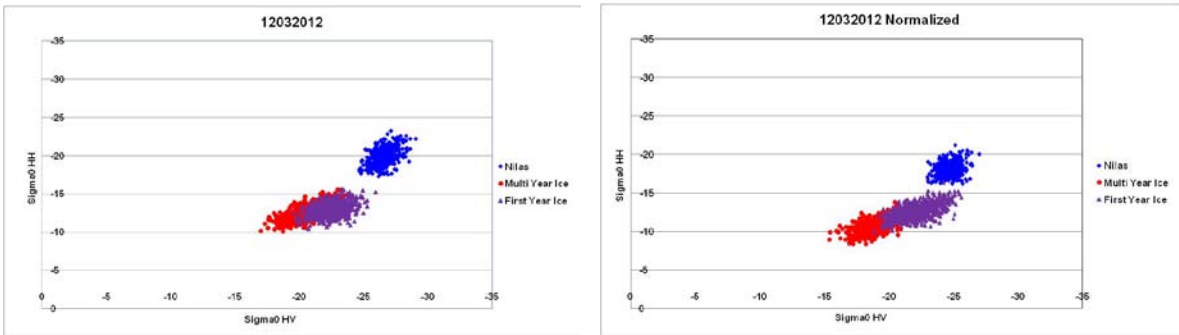

Figure 2-6 Graphs showing sigma-naught values for HH- and HV-polarization extracted from the image of March 12, 2012, (left) before normalization and (right) after normalization

The graphs show that sigma-naught at HH-polarization for nilas is ranging between -30dB and -15dB, changing after normalization. The change depends on the difference between the normalization angle and the incidence angle at which the ice type is actually observed. At HV-polarization backscattered intensity is lower in most cases by about 5dB. Sigma-naught at HH-polarization for multiyear ice is around -10dB to -15dB, the values do not change significantly after normalization. At HV-polarization, intensity variations are larger (about -15dB to -25dB). First-year ice intensities are shifted to lower intensities by 3dB to 7dB at HH-polarization but only at maximum 2dB at HV-polarization. From these graphs we see that nilas is well separated from the other two types, while the first-year ice and multiyear reveal overlaps in their intensity values. These overlaps make it difficult sometimes to separate these two types.

2.2.3 Classification

In this section we present the results of simple trials to classify the normalized images from the previous section. Two of these images are presented in Figures 2.7 and 2.8. A segmentation routine available through ERDAS IMAGINE software was used here. It partitions raster images into segments based on the pixel values and the pixel locations. The result is a thematic image in which pixel values represent class ID's of contiguous raster objects. Here we used the three defined ice types.

The method shows good separation between ice and water, which is demarcated here with the yellow line. The results (classified images) also show the influence of an image artifact that occurs at HV-polarization (stripe parallel to the azimuth direction). The HV-polarization is not improving the ice classification as expected from the results shown in Figs. 2.4-2.6. The stripes need to be removed or

reduced because they can influence the classification. HV-polarization improves the separation between water and sea ice, which is demonstrated in Figs. 2.7 and 2.8 where the ice edge is clearly defined. This is also demonstrated also in Figure 2.9 But the HH-polarization channel is more sensitive to new ice compared to HV polarization channel (Figure 2.10).

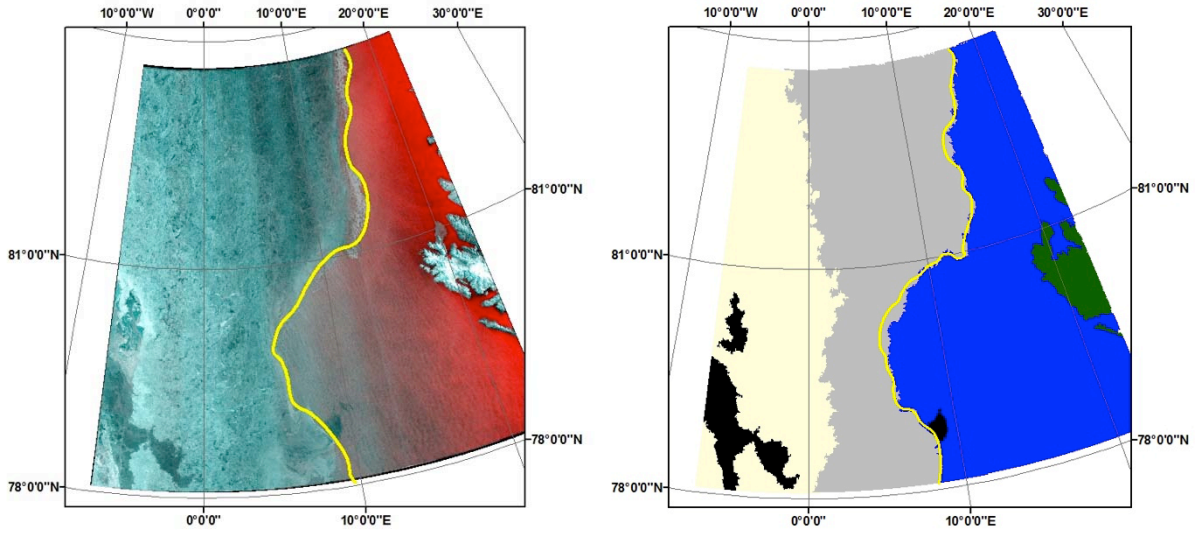

Figure 2-7 Radasat-2 image dated from March 12, 2012, (left) HH and HV polarization projected in RGB, (right) segmentation result, green color represent land, blue water, grey first year ice, beige multiyear ice, and black is nilas.

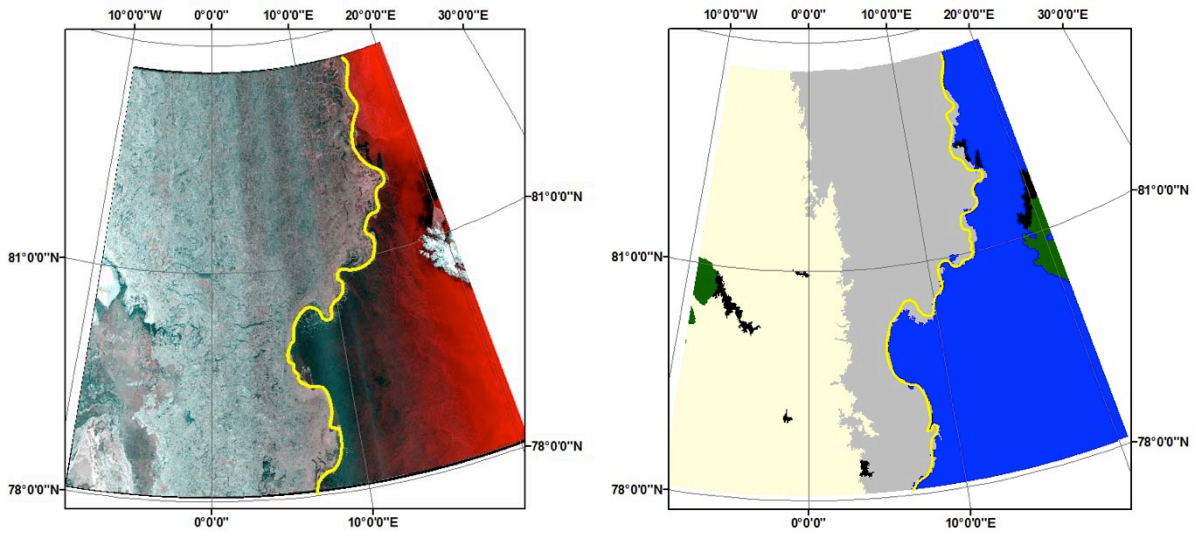

Figure 2-8 Radasat-2 image from March 22, 2012, (left) HH and HV polarization projected in RGB, (right) segmentation result, green color represent land, blue water, grey first year ice, beige multiyear ice and black is nilas.

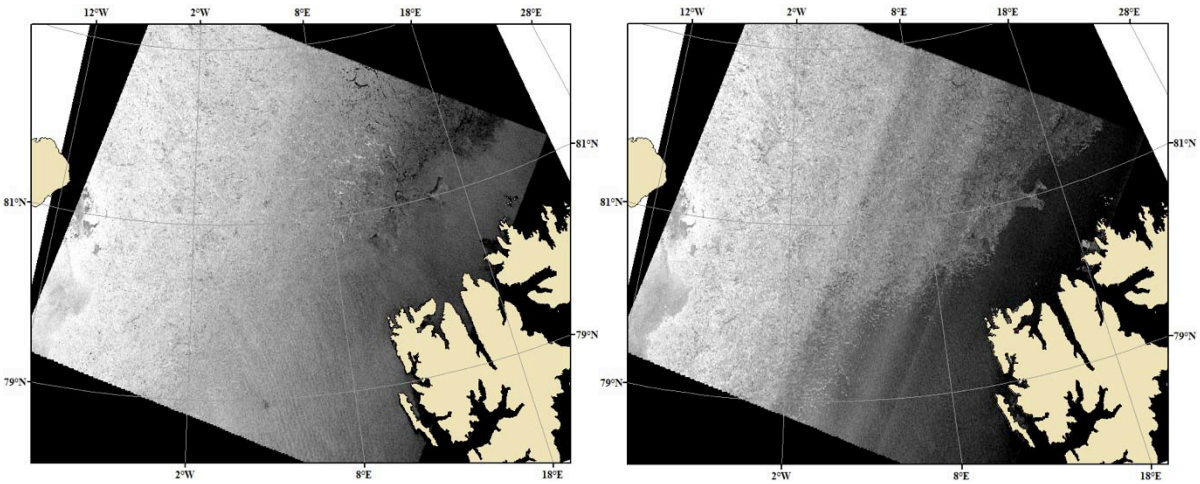

Figure 2-9 Radarsat-2 image from February 24, 2012, (left) HH polarization and (right) HV polarization. The latter shows better detection for the ice edge compared with HH polarization.

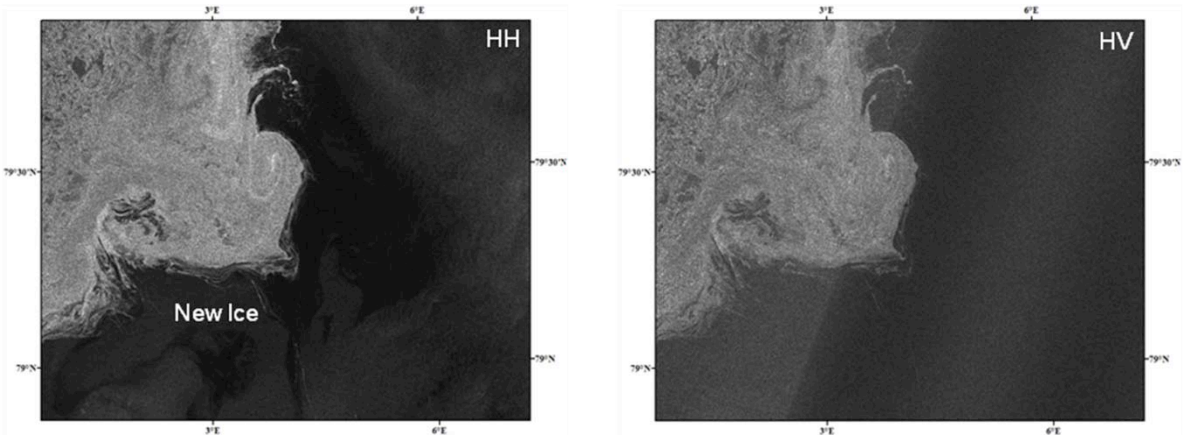

Figure 2-10 Radarsat-2 image from 5 April 2011, (left) HH polarization and (right) HV polarization. HH is more sensitive to new ice than HV.

2.3 Automatic ice-water discrimination in Radarsat-2 dual polarisation images

Anton Korosov, Natalia Zakhvatkina, Torill Hamre, Stein Sandven (NERSC, NIERSC)

An automatic procedure for Radarsat2 data processing and daily mapping of ice in the Barents Sea (around Svalbard) at 1 km spatial resolution has been developed and run autonomously. All RADARSAT-2 data available within MyOcean2 project are downloaded from the GMES DWH to the NERSC server, uncompressed and processed first at Level 2 (image-per-image ice/water classification) and then at Level 3 (daily maps generation). We use data from RADARSAT-2 received in ScanSAR Wide (SCW) mode at dual-polarization, i.e. HH (horizontally transmitted and horizontally received) and HV (horizontally transmitted, vertically received). This mode assembles wide SAR image from several narrower SAR beams, resulting to an image of 500 × 500 km with 50 m resolution.

A non-linear scheme for classification of RADARSAT-2 data has been developed. The processing allows to identify three classes: ice, calm water and rough water at 1 km spatial resolution. The raw sigma0 data in HH and HV polarization is used for computing texture characteristics in a moving window

using a Gray Level Co-occurence Matrix (GLCM). A neural network is applied at the next step for processing array of the most informative texture characteristics and ice/water classification. Examples of ice-water discrimination are shown in Fig. 2.11 and Fig. 2.12.

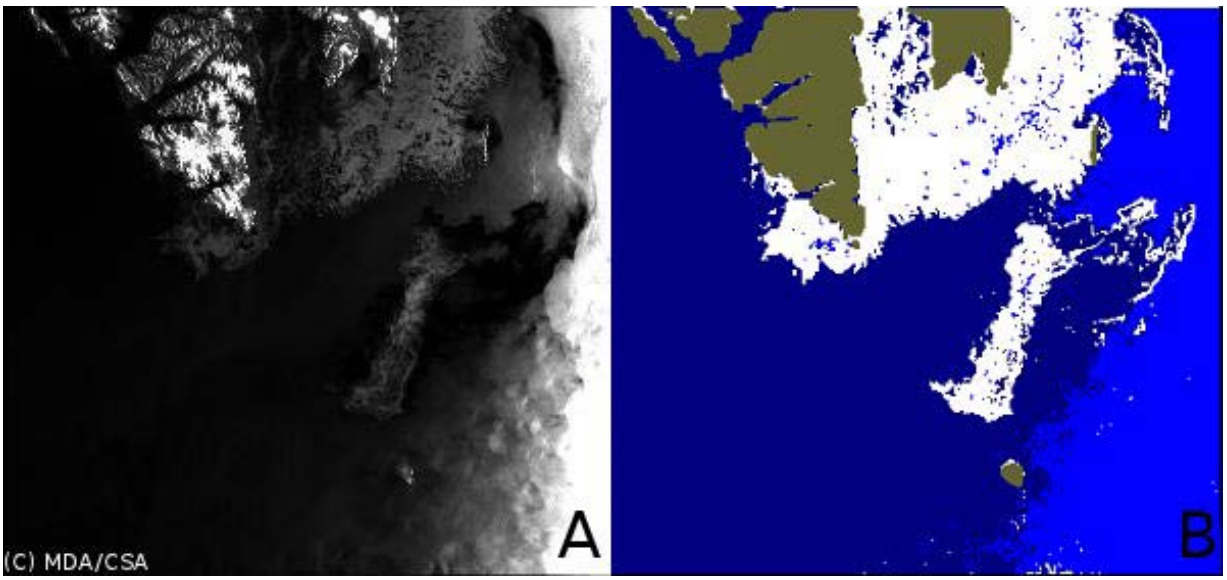

Figure 2-11 An example of Radarsat2 image (A) classification (B) into ice (white), calm water (dark blue) and rough water (blue). Greenish color masks land (Svalbard on top and Bear-island near bottom on this image).

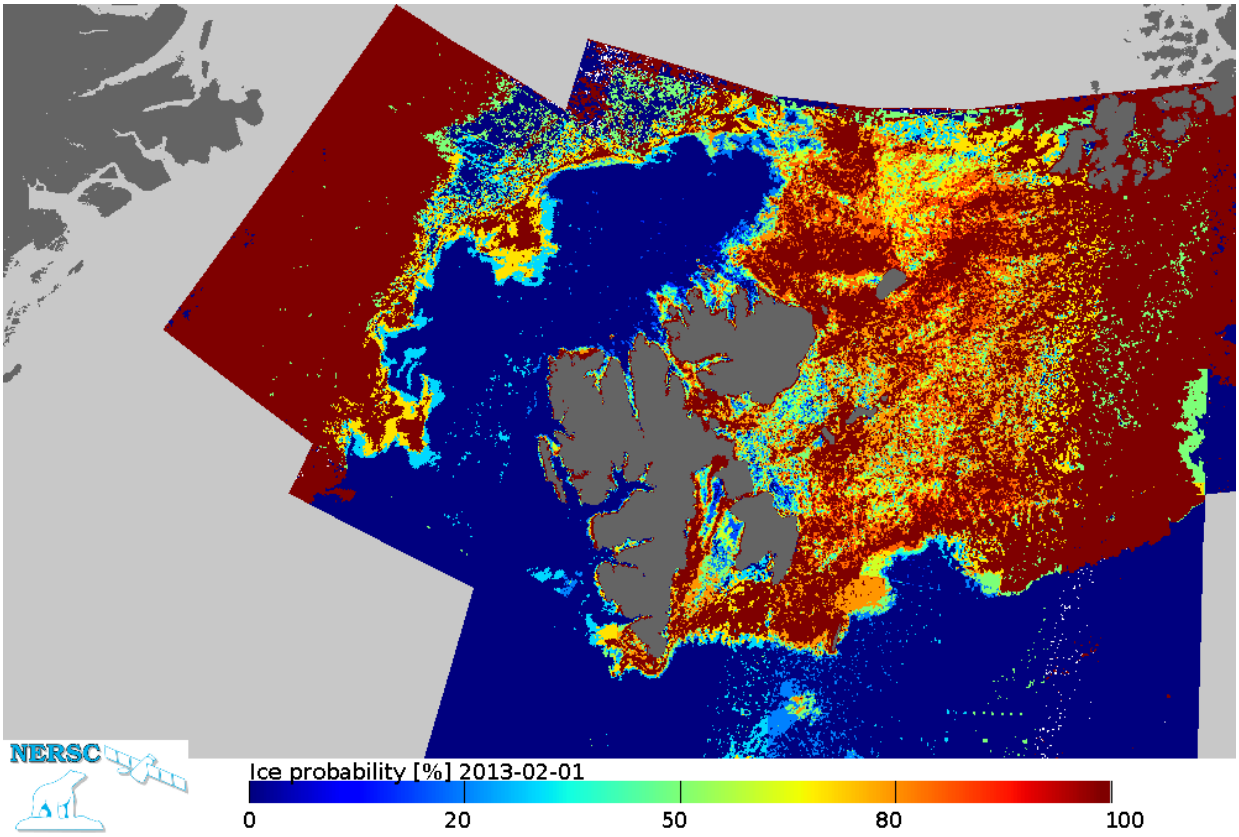

Figure 2-12. Example of sea ice classification map averaged over 7 days for February 2, 2013.

The main results so far are:
* the most informative texture characteristics to be used for sea ice classification were revealed;
* the best set of parameters including the window size, number of levels of quantization of sigma0 values and co-occurence distance was found;
* a neural network was trained on results of visual classification of 30 RADARSAT-2 images.

Despite the general high accuracy of the neural network (90% of true positive classification) problems with classification of young newly formed ice and rough water arise due to the similar average backscatter and texture, presence of thermal and random noise. Methods of removal of thermal noise, smoothing and computation of texture characteristics (e.g. computation of GLCM from a variable size window) will be assessed in future.

A web-site for accessing L2 and L3 results of RADARSAT-2 processing has been established. Results of classification are also provided to the Norwegian Meteorological Institute in NetCDF/CF files are available online.

2.4 Classification in ENVISAT SAR images using Bayesian and Neural Network algorithms

N. Zakhvatkina, V. Y. Alexandrov, and E. V. Shalina, NIERSC

Analysis of sea ice in SAR images can be done with a number of different techniques. Developing automatic ice classification methods for SAR images has been a long-standing goal for sea ice researchers at NIERSC.

The objective of sea ice classification of SAR images is to identify the main sea ice features related to ice types and surface roughness and classify them into a set of pre-defined categories that should be in agreement with the sea ice nomenclature as defined by the World Meteorological Organization (WMO) [Rep. 259, 1989]. This implies that quantitative information about forms of ice, stage of development and concentration should be derived from SAR images. This information is routinely derived by visual inspection of SAR images in production of operational ice charts, but this process may possibly be improved by use of automatic algorithms.

The most straightforward method to employ SAR data for sea ice analysis is to use backscattering coefficients (σ°) for discrimination between multiyear, first-year and some young and new ice types, but this method is hampered by ambiguities in the relation between ice types and σ° [Johannessen et al., 1997; Abreu, 2000], since different ice types can have similar σ° [Sandven et al., 1999; Dierking, 2010]. Including additional image characteristics such as image texture and others into the analysis improves the classification results.

The main objective of the NIERSC research within SIDARUS Project has been developing a neural network (NN)-based sea ice classification method for SAR images, including its comparison with Bayesian approach and validation. The NN-based algorithm is developed to discriminate between Level First-Year (LFYI), Deformed First-Year (DFYI), Multiyear ice (MYI) and Open water/Nilas (ON) in the high Arctic during winter conditions. The study includes the following steps:

1) to determine the backscattering coefficients or the Normalized Radar Cross Section from ENVISAT Wideswath SAR images (C-band, HH-polarization) for the four afore-mentioned ice types based on a selected data set from the interior of the Arctic;
2) to estimate σ° as function of incidence angle from the data set and normalize it to a fixed angle for each ice type;
3) to investigate and select the optimal combination of SAR image texture characteristics for discrimination between the ice types;
4) to train the NN-based algorithm using the σ° and the selected texture parameters and perform classification of a test data set using the NN-algorithm;
5) to carry out sea ice classification using trained NN;
6) to compare the NN-algorithm classification results with a Bayesian classification and to validate it by using independent data.

2.3.1 Data preprocessing

A series of 14 ENVISAT ASAR WS images (pixel spacing 75 m × 75 m, 420 km swathwidth) at HH-polarization, acquired over different Arctic regions in winters of 2005 and 2006, were used for analysis of the sea ice backscatter σ°. The backscatter coefficients for five sea ice types (ON, young ice, LFYI, DFYI, and MYI) were derived for an incidence angle of 23°. This angle was selected for comparison with literature data on sea ice backscatter at VV-polarization, mostly derived from ERS SAR images. Mean and ranges of σ° for the five ice types were calculated. Our results are in good agreement with previously reported σ° values and the analysis confirms like earlier studies that additional image features need to be used in automatic sea ice classification in SAR images.

As to angular dependency of the sea ice backscatter for different ice types, it was derived from 8 ENVISAT ASAR Wideswath calibrated images suitable for the task. In order to classify SAR images where σ° is a function of incidence angle, the σ° values have been normalized across the swath, using 25° as a reference angle and a linear function for the predominant ice type.

2.3.2 Bayesian and Neural Network (NN) algorithms

The first method applied in this study for sea ice classification is the Bayesian algorithm. We believe that Bayesian algorithm is suitable for the Central Arctic, where MYI dominates, so its a priori probability is quite high. In this study the Bayesian classification was mostly used for comparison with NN classification.

The elaborated algorithm is pixel-based and uses a priori probability of occurrence of given ice types. A posteriori probability $p(\omega_j/x_i)$ for various sea ice classes is calculated as [Duda and Hart, 1973]:

$$p(\omega_j / x_i) = p(x_i / \omega_j) \times p(\omega_j) \big/ p(x_i) \quad \text{,where}$$

$$p(x_i) = \sum_{j=1}^{N} p(x_i / \omega_j) \times p(\omega_j)$$

Here $p(\omega_j)$ – a priori probability, $p(x_i/\omega_j)$ – conditional probability of x_i for class ω_j.

The conditional probabilities $p(x_i/\omega_j)$ were assessed from calibrated ENVISAT Wideswath SAR images, where areas typical for each ice type were delineated visually. Statistically significant estimates of conditional probabilities were derived for MYI, DFYI and LFYI. Due to the absence of reliable estimates of conditional probabilities for ON and young ice we made an assumption that mainly only three ice types (MYI, LFYI, and DFYI) are observed in the central Arctic and their a priori probabilities are 0.9, 0.05, and 0.05, respectively. Here we also assume that leads in the MYI are covered with LFYI. Classification was carried out for the three mentioned ice classes.

Decision is made in favour of:

ω_{my}, if $p(\omega_{my}/x_i)>p(\omega_{fy}/x_i)$ and $p(\omega_{my}/x_i)> p(\omega_{fd}/x_i)$

ω_{fy}, if $p(\omega_{fy}/x_i) > p(\omega_{my}/x_i)$ and $p(\omega_{fy}/x_i) > p(\omega_{fd}/x_i)$

ω_{fd}, if $p(\omega_{fd}/x_i) > p(\omega_{my}/x_i)$ and $p(\omega_{fd}/x_i) > p(\omega_{fy}/x_i)$

The neural network (NN)-based algorithm is the second approach used for sea ice classification. The NN-algorithm uses both backscatter and textural characteristics of the images. Several studies have shown that SAR sea ice classification accuracy is improved by using image texture features [Bogdanov et al., 2005; Hara et al., 1994]. Texture features describe spatial variations of image brightness within a group of neighboring pixels large enough to calculate statistically significant estimates. A given texture feature can be different from one ice type to another and reflect variability in sea ice properties sensed by the SAR.

After σ° normalization to 25° incidence angle eight texture features - correlation, inertia, cluster prominence, energy, homogeneity, and entropy, as well as 3rd and 4th central statistical moments of image brightness were calculated in this study. That has been done for a set of images representing relatively homogeneous areas of each of the four ice types in the study (LFYI, DFYI, MYI and ON). Ice type ON represents a mixture of new ice (grease ice), nilas and calm open water, which all have a low backscatter and therefore cannot be further discriminated without additional data. Statistical analysis showed that the entire set of selected texture features can be used for discrimination of the four ice types. Therefore, all eight texture-features mentioned above and the backscatter coefficients were used as input for creation, training and determination of the NN parameters.
The NN algorithm belongs to the group of supervised training methods of classification. In our case, the training phase of the NN was based on the back-propagation learning rule. The NN algorithm was trained for sea ice classification in the high Arctic during winter conditions.

The optimal NN topology for ENVISAT ASAR sea ice image classification was selected based on the analysis of ice expert's classified input data as well as on processing time. The selected topology consisted of nine neurons in the input layer, which correspond to the number of used features, six neurons in the hidden layer and three neurons in the output layer. The output neurons correspond to classes of LFYI, DFYI and MYI. The trained NN was applied to the training data set to check if the ice classes initially defined in the training data set could be reproduced. The correspondence was 96.7% for MYI, 98% for DFYI, and 97% for LFYI. This test suggested that the NN classification algorithm is self-consistent. Another NN was trained to classify ON, LFYI, DFYI and MYI types using ON areas, delineated in the same SAR images in addition to the previously determined datasets of LFYI, DFYI and MYI. Optimal topology of this NN consists of nine, fifteen, and four neurons in input, hidden, and output layers, respectively.

The trained NNs were applied for automated classification of 20 ENVISAT ASAR images that were not used in the training/testing procedure. Each SAR image was first preprocessed with the angular correction for the predominant ice type for an incidence angle of 25°, after that texture characteristics for the whole image were calculated and in the end NN classification of sea ice types was done. Classification with the NN algorithm was carried out for LFYI, DFYI and MYI, and in the case of second NN also for ON for the central Arctic.

2.3.3 Results of classification

The trained NN was tested by classification of SAR images used for training. The results of classification were compared with AARI (Arctic and Antarctic Research Institute, Russia) ice charts (www.aari.ru), which depict the distribution of open water and sea ice types - nilas, young, first-year and old ice during winter period (1.XI-31.V). These charts are based on the generalization of regional ice charts, compiled from visible, infrared and radar satellite images and reports from coastal stations and ships. The classification results were also compared to the ice analysis of the same SAR images performed by ice experts at AARI. The ice experts estimated visually the partial concentration for each ice type corresponding to the NN classes. This partial concentration was then compared with the partial percentage of each ice class from the NN analysis. The percentage of correspondence between the NN classification, ice charts and expert analysis for the whole classified image has been presented in the confusion matrixes (main diagonal in Table 2.3 and Table 2.4).

Table 2-3 Main diagonal of the confusion matrixes for comparison of classification results, applied to ENVISAT ASAR images, used for NN training/testing and Bayesian approach, with AARI ice charts

SAR images, used for Bayesian classification and NN training / testing	Accuracy (NN with AARI ice chart zones – MYI and FYI),%		Accuracy (Bayes with AARI ice chart zones – MYI and FYI), %	
Date\ Time (UTC)	**MYI**	**LFYI+ DFYI**	**MYI**	**LFYI+ DFYI**
01 March 2004 \ 01:00	no AARI ice chart			
06 December 2005 \ 16:28	85.8	95.2	79.0	98.2
15 January 2006 \ 15:32	82.3	83.1	87.0	97.1
06 March 2006 \ 15:58	no AARI ice chart			
31 March 2006 \ 16:14	85.3	97.0	40.1	96.2
01 April 2006 \ 17:20	91.0	91.0	68.2	98.7
18 April 2006 \ 06:58	68.2	87.4	63.3	93.5
07 December 2007 \ 11:54	87.6	93.4	89.8	99.4
09 January 2008 \ 09:38	64.5	89.6	61.3	88.2
16 January 2008 \ 07:36	76.6	95.2	51.0	95.3
06 February 2008 \ 09:56	63.36	99.9	79.5	91.6
11 December 2008 \ 01:21	89.3	90.5	61.1	89.7
Total accuracy	**79.3**	**92.2**	**68.1**	**95.6**

Table 2-4 The confusion matrixes for comparison of NN and Bayesian classification results, applied to ENVISAT ASAR images, with visual experts estimation a) 18.01.2008 (Fig. 2-13 c) and b) 04.02.2008 (Fig. 2-14 c)

January 18, 2008

		Vsual expert analisys zone * :			
		C	A	B	D
NN class. result	MYI	64.76	6.49	25.37	3.39
	LFYI	0.87	86.18	10.95	1.99
	DFYI	1.26	23.58	73.49	1.67
	ON	12.98	34.77	14.06	38.19
Bayes class. result	MYI	52.38	8.27	39.36	7.23
	LFYI	0.51	94.36	5.13	70.9
	DFYI	0.82	74.29	24.89	21.86

* SAR image was divided into zones of 4 ice types visually by sea ice experts (Fig. 1 b): A is LFYI, where ridges cover less then 20% of ice surface, B is first-year ice, where ridges cover more than 20% of ice surface, C is MYI area, and D is ON. The ice types inside each zone were missed.

(a)

February 04, 2008

		Vsual expert analisys zone ** :		
		C	A	B+D
NN class. result	MYI	72.15	2.46	25.35
	LFYI	0.71	62.08	37.19
	DFYI	15.61	11.06	73.29
Bayes class. result	MYI	67.96	2.46	29.59
	LFYI	0.47	73.14	26.39
	DFYI	14.17	29.93	55.90

** SAR image was divided into zones of 3 ice types visually by sea ice experts (Fig. 2 b): A is LFYI, where ridges cover less 20% of ice surface, B is first-year ice, where ridges cover more than 20% of ice surface, C is MYI area, and D is thick FYI and second-year ice. The ice types inside each zone were missed

(b)

An example of classification results is shown in Fig. 2.13 where the SAR image from January 18, 2008 covers the transition zone between MYI and FYI north of the Barents Sea. The image was divided into zones of four ice types: A is LFYI, where ridges cover less than 20% of ice surface, B is first-year ice, where ridges cover more than 40% of ice surface, C is MYI area, and D is ON (Fig. 2.13 b). The result of the NN classification is shown in Fig. 2.13 c with the ice expert's analysis superimposed. The confusion matrix between classification results and expert analysis gives 86%, 73%, 65%, and 38% correspondences in areas A, B, C, and D, respectively (Table II a). This is a relatively good result because the ice structure is very complex and the expert analysis does not take into account all the small features in the image. The result also shows difficulties in separating ON from LFYI, although some ON in leads could be classified in the MYI region (area C). The backscattering from open water, nilas and LFYI can be similar and in some cases experts cannot distinguish them in SAR images without additional information. Therefore our further analysis deals with the classification of three ice types - LFYI, DFYI and MYI.

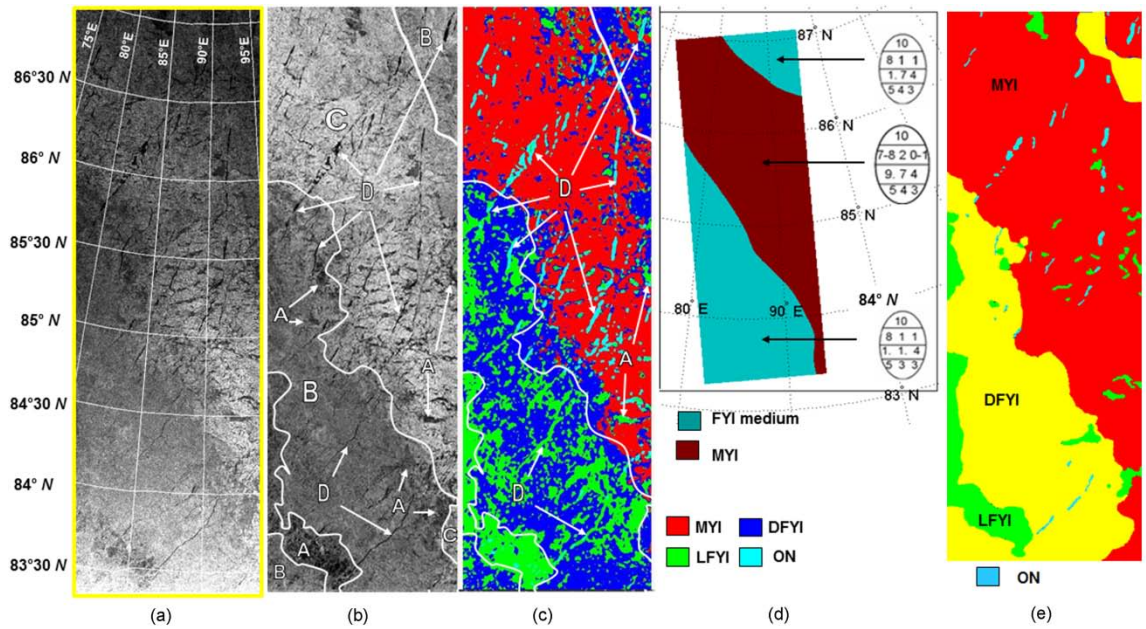

Figure 2-13 (a) Part of original ENVISAT Wideswath SAR image (HH–polarization), taken over north of the Kara Sea on January 18, 2008 at 09:55 UTC; (b) part of SAR image with normalized σ° to incidence angle of 25° and analysis by an ice expert from AARI: A is LFYI, where ridges cover more than 40% of ice surface, C is MYI area, and D is ON. Arrows show location of small ice features, marked by corresponding characters; (c) result of the NN classification of four ice types where the class ON is included; (d) ice chart provided by AARI for January 16-18, 2008. The lower legend is for the SAR classification and the upper legend is for the ice chart; e) manually colored image according to sea ice expert's visual analysis.

Another SAR image for February 4, 2008 covering the transition zone from FYI to MYI, was classified using three ice types (Fig. 2.14 a). The experts delineated areas marked as: (A) - LFYI, where ridges cover less than 20% of ice surface; (B) - DFYI, where ridges cover more than 40% of ice surface; (C) - MYI area; and (D) - thick first-year ice and second-year ice. The NN classification gave 72% correspondence with expert analysis in area C with predominantly MYI. In areas A and B+D correspondences between NN classification and expert analysis was 62% and 73%, respectively (Table 2.3 b). The expert analysis suggested that second-year ice or smaller forms of MYI are present in area D. The NN was not trained to classify this ice type and would therefore tend to classify these areas as MYI or DFYI.

The results of NN classification were also compared with digital ice charts (Fig. 2.13 and 2.14, d), where only one FYI class is used. This implies that LFYI and DFYI from the NN classification cannot be validated separately, but jointly as one class. This joint class corresponds to first-year ice shown in ice charts by 93% and 99%, respectively. The MYI result shows a correspondence of about 64% and 46%, respectively. However, the MYI area is not very accurately estimated in the ice charts because information comes mainly from visible and IR satellite images.

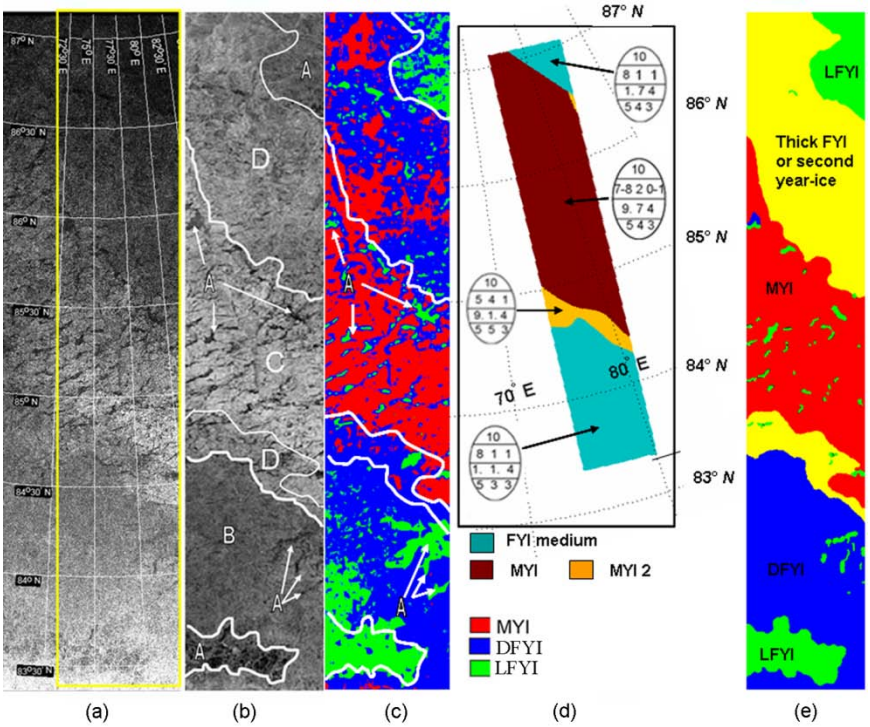

Figure 2-14 (a) Part of original ENVISAT Wideswath SAR image (HH–polarization), taken over the northern part of Kara Sea on February 04, 2008 at 11:00 UTC with geographical grid where near-range is in the lower part and far-range in the upper part, where yellow box shows a classified part of the image; (b) part of SAR image after normalization of σ° to incidence angle of 25° and analysis by an ice expert from AARI: A is LFYI, where ridges cover less 20% of ice surface, B is FYI, where ridges cover more than 40% of ice surface, C is MYI area, and D is thick FYI and second-year ice. Arrows show location of small ice features, marked by corresponding characters; (c) the result of NN classification; (d) ice chart provided by AARI for February 06, 2008. The lower legend is for the SAR classification and the upper legend is for the ice chart; (e) manually colored image according to sea ice expert's visual analysis.

The best method available in this study is the expert analysis (Fig. 2.13 and 2.14, e), because the expert has spent time to analyze the SAR images in more detail. The average correspondences in NN and expert classifications, calculated from this series of ASAR images amount to 85%, 83%, and 80% for LFYI, DFYI and MYI, respectively. The NN consistently distinguishes MYI areas from those with predominantly first-year ice. Within larger areas of MYI it identifies wide leads, although ice type in leads could be misclassified in some cases.

Twelve ENVISAT ASAR images, acquired in the Central Arctic, were also classified using Bayesian algorithm in order to compare classification results from two different methods. The pre-processing of the SAR images is similar to the NN-method and consists of calibration, normalization to incidence angle of 25°, and also speckle reduction. Confusion matrices have been calculated to compare the classification results of the Bayesian algorithms with ice charts.

A comparison of classification by the two algorithms is illustrated in Fig 2.15. The Bayesian algorithm was applied twice to this image shown in Fig. 2.15 a, first with a 4 × 4 pixel resolution (Fig. 2.15 c) and then averaged by 32 × 32 pixels to present a classified image with the same resolution as the NN algorithm (Fig. 2.15 d). The classification results look quite similar (Fig. 2.15 b, c, d) and higher

resolution provides a more detailed classification, allowing better detection of leads and other small-scale features. On the other hand, the higher resolution also implies more noise in the classification results. The lower resolution shows results that are comparable to the NN results.

Comparison of Bayesian classification results for images shown in Fig. 2.13 and 2.14 with visual expert analysis is presented in Table II. The total classification accuracy was 52.4% and 67.9% for MYI; 73.1% and 94.4% for LFYI; 24.9% and 55.9% for DFYI, respectively. Poor accuracy in DFYI classification may be explained by problems in subjectivity distinguishing LFYI from DFYI in the process of SAR image visual interpretation.

The main result is that MY ice and FY ice were generally identified correctly by both methods. The major difference is that Bayesian method shows larger area of LFYI, whereas the NN method shows predominance of DFYI. There is no validation data to provide evidence which ice type is predominant. Both methods show wide leads in MYI, but the Bayesian method seems to classify ice in the leads as LFYI, which is more correct than DFYI from the NN method. This misclassification may be caused by using sliding window for textural characteristics calculation in the NN algorithm. The size of this sliding window is comparable with typical size of small-scale ice features. In case of Bayesian classification, lower values of σ° for LFYI and higher values for MYI tend to be averaged within the sliding window and the resulting value appear as DFYI. Bright narrow features in area of first-year ice are leads with frost flowers. They were mostly classified as MYI, because the Bayesian algorithm does not include young ice, since its backscatter is similar to that of MYI.

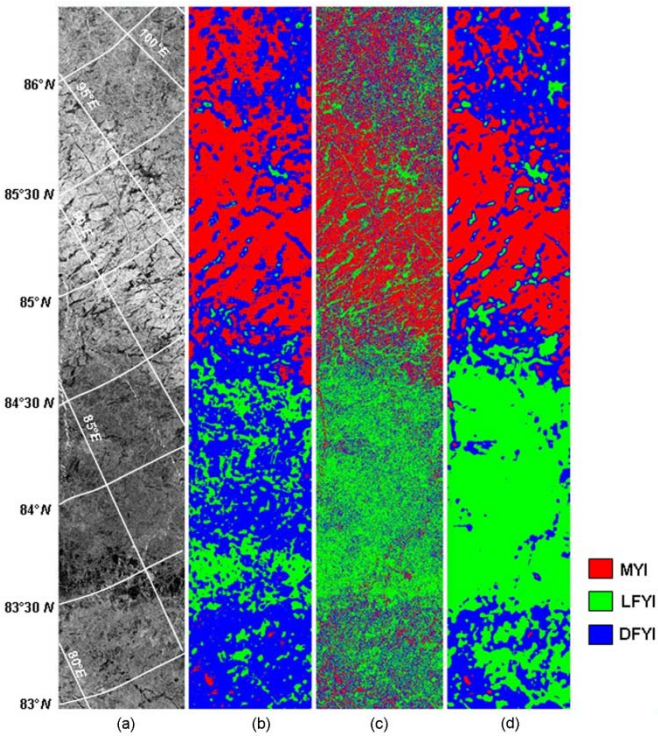

Figure 2-15 Sea ice classification of original ENVISAT Wideswath SAR image (HH–polarization), taken over the NP-35 area, north of Barents Sea on January 14, 2008 at 11:59 UTC. (a) part of SAR image with σ° normalized to incidence angle of 25°; (b) result of NN classification for 3 sea ice types; (c) Bayesian approach classified image; (d) Bayesian approach classified image by averaging with a sliding window of 32×32 pixel and a moving step equal to 4 pixels.

2.3.4 Conclusions

The classification results of 12 trainig images were compared with ice charts issued by the Arctic and Antarctic Research Institute, where multiyear ice and first-year ice were discriminated. The total classification accuracy, determined by the confusion matrix between classification results and ice charts, was 79.3 % for multiyear ice, and 92.5 % for first-year ice in case of NN classification; and 68.1% for MYI, and 95.7 % for FYI using Bayesian algorithm.

A series of 20 ENVISAT ASAR images of sea ice was classified using Bayesian and the NN algorithms. The images were selected as representative for winter sea ice in the Central Arctic. It has been shown that the NN algorithm can distinguish multiyear ice from areas with predominant level first-year ice, deformed first-year ice and open water / nilas. Within areas of multiyear ice it can also identify relatively wide leads, whereas classification between open water, nilas and other thin ice types was not attempted. To simplify the classification, open water and nilas were treated as one ice type, characterized by lower backscatter than the other ice types. The average correspondences in NN classification of ASAR image series, as compared with visual expert's estimates, amount to 85%, 83%, and 80% for level, deformed first-year ice and multiyear ice, respectively.

The Bayesian classification algorithm uses a priori probabilities of level, deformed first-year ice and multiyear ice appearance in the Central Arctic. These probabilities were estimated from knowledge of ice conditions, and conditional probabilities of these ice types were derived from calibrated ENVISAT ASAR WSM images. The Bayesian algorithm uses only backscatter, but correctly classifies major sea ice types due to big differences in their a priori probabilities, as well as leads in sea ice. A comparison of confusion matrixes shows a correspondence of Bayesian and NN classification results for level first-year ice and multiyear ice in the Central Arctic. In this case when both data sets are not perfect it is possible to estimate the difference between the two data sets and not the error. Correspondence of these two algorithms is from 97.8 % to 99.1 % for FYI, from 48.7% to 73.9% for DFYI, and from 47.1 % to 87.8 % for MYI. The NN classification results are less noisy, whereas pixel-by-pixel Bayesian algorithm better detects narrow leads in the ice cover. NN allows detecting wide leads, which are important for climate studies and ice navigation.

Classification accuracy can be improved by using SAR images at different polarizations and the next step of this study is development of sea ice classification from multipolarization data. The automatic SAR ice classification can be done using data from RADARSAT-2.

References

1. World Meteorological Organization, WMO Sea Ice Nomenclature, Geneva, WMO Rep. 259, 1989.
2. O. M. Johannnessen, A. Volkov, V. Grischenko, L. Bobylev, V. Asmus, T. Hamre, K. Kloster, V. Melentyev, S. Sandven, V. Smirnov, J. Solhaug, and L. Zaitsev, "ICEWACH: Ice SAR monitoring of the Northern Sea Route," in Operational Oceanography: The Challenge for European Cooperation - Proc. of the First Int. Conference on EuroGOOS, 7-10 Oct. 1996, J. H. Stell, H. W. A. Behrens, J. C. Borst, L. J. Droppert, Eds. Elsevier, The Hauge, The Netherlands: Elsevier Oceanography Series № 62, 1997, pp. 224-233.

3. R. D. Abreu, “RADAR Sea Ice Signatures: An Operational Primer,” in Proc. Workshop on mapping and archiving of sea ice data – the expanding role of radar, Ottawa, Canada, May 2-4 2000. JCOMM Tech. Rep. № 7, pp. 85-94, 2000.
4. S. Sandven, O. M. Johannessen, M. W. Miles, L. H. Pettersson and K. Kloster, “Barents Sea Seasonal Ice Zone Features and Processes from ERS–1 Synthetic Aperture Radar: Seasonal Ice Zone Experiment 1992,” J. Geophys. Res., vol. 104, no C7, pp. 15843–15857, Jul. 1999.
5. W. Dierking, “Mapping of Different Sea Ice Regimes Using Images From Sentinel-1 and ALOS Synthetic Aperture Radar,” IEEE Trans. Geosci. Remote Sens., vol. 48, no. 3, pp. 1045-1058, Mar. 2010.
6. R. Duda and P. Hart, Pattern Classification and Scene Analysis. New York: Willey, 1973.
7. A. Bogdanov, S. Sandven, O. M. Johannessen, V. Alexandrov, and L. Bobylev, “Multisensor Approach to Automated Classification of Sea Ice,” IEEE Trans. Geosci. Remote Sens., vol. 43, no 7, pp. 1648–1664, Jul. 2005.
8. Y. Hara, R. G. Atkins, R. T. Shin, J. A. Kong, S. H. Yueh, and R. Kwok, “Application of Neural Networks to Radar Image Classification,” IEEE Trans. Geosci. Remote Sens., vol. 32, no 1, pp. 100–109, Jan. 1994.

3 SAR iceberg analysis using a dedicated processing chain

N. Longépé and P. Fabry, CLS

3.1 Introduction

SAR-based technology has been operationally used by CLS for years to provide an integrated monitoring system for iceberg detection in Antarctica during solo-round-the-world races (for instance the Vendée Globe and the Jules Verne Trophy) (See Longépé et al. 2012). The system integrates SAR-based observation and detection, oceanographic data, sailboat record and a drifting model. To cover the sailboats all along the Antarctica circumnavigation, Wide Swath Medium resolution mode of the ASAR/ENVISAT satellite were used. This mode is adequate to cover wide areas with a swath width of 400 km, while maintaining a sufficient resolution (150 meters) to detect Antarctic icebergs.

For this study aiming at detecting Arctic icebergs in the Barents Sea, the SAR-based methodology for iceberg detection must be further modified so as to monitor far smaller icebergs either trapped in sea ice or free in open water.

3.2 Status prior SIDARUS

SARTool© is a powerful software designed to produce value-added information from SAR scenes acquired by various satellite missions (ERS-1/2, ENVISAT, RADARSAT-1/2, COSMO SkyMED, TerraSAR-X, etc.). This IDL-based user friendly software has been designed by CLS engineers to provide analysts with the capability to support intuitive and efficient handling and processing of any type of path-oriented SAR images.

Based on the current highest level of physical understanding of the SAR imaging mechanisms, SARTool© proposes efficient solutions to monitor man-made activities and natural processes on the sea surface using the most advanced retrieval algorithms.

SARTool© has a modular architecture consisting of a core GUI (SARTool Explorer) and a suite of single applications modules. The objective of each module is to reduce the amount of data contained in SAR images to the most precise and useful information. These modules allow various type of analysis, from ships/icebergs or oil detection to wind/swell/wave retrieval.

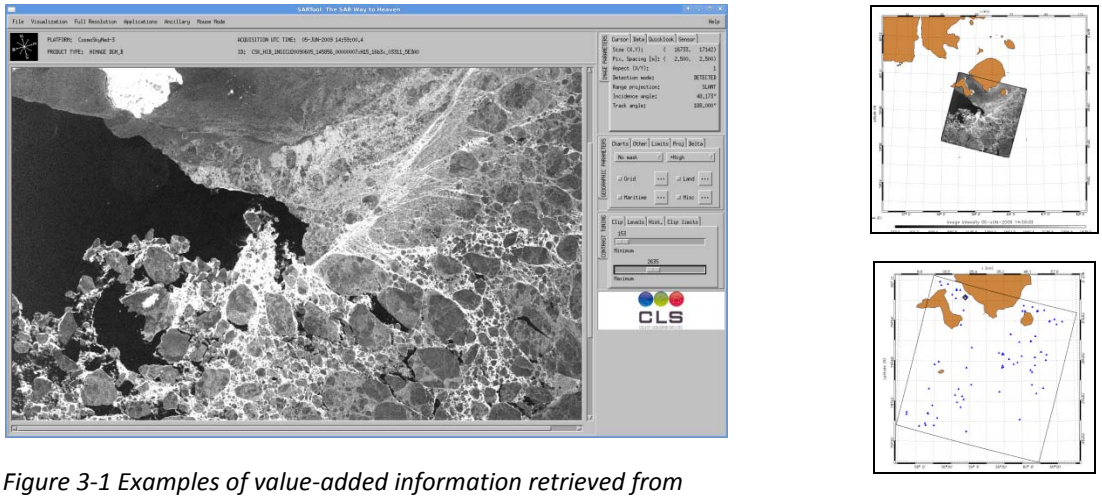

Figure 3-1 Examples of value-added information retrieved from SAR images by SARTool

The automatic bright-target detection scheme in SARTool© is carried out as follows:

- Land masking: A mask is obtained from a dedicated coastline database. An exclusion area is also applied which enables geo-localization problems to be handled during the processing (lack of accuracy of the database, tide effects).

- Pre-screening phase by adaptive threshold using a sliding window: A threshold is applied using a sliding window assuming a Constant False Alarm Rate (CFAR). This rule is applied on a pixel-basis.

- Classification: This step is of high importance to remove false alarms. It includes artifact detection linked to the acquisition geometry (range/azimuth ambiguities), the SAR image formation (secondary lobes in radial and azimuthal direction, scalloping) and the sensor itself (thermal noise). The real differentiation between SARTool and other SAR-based detection software is made through this post-processing step.

The use of a CFAR-based methodology is of high interest over homogeneous areas (such as open water) but may be less powerful over heterogeneous regions. Sea ice conditions in the Barents Sea are highly complex (e. g. various ice types of different age, deformation stage), especially in the ice edge region which is subject to different processes (compaction and relaxation due to wind, freezing and thawing). Its SAR signature also depends on incidence angle, polarization and sensor frequency. That is why the supervision by a trained analyst is strongly required in the case of complex Arctic environment. CLS developed a new module for this supervised step.

In addition to these aforementioned automatic processes, SARTool icebergs annotations workflow is displayed on screen for the analyst. This workflow is based on the SARTool Explorer, with some additional capabilities. On the start-up of the screen, the result of the bright target detection is made available on the image to the analyst. Then he can start the analysis, tag some of the reliable or non-reliable targets, or delete the false detections. The analyst can also draw on the image the huge icebergs (over 100m long) and areas of interest: ice pack, high/low density. The result of the analysis can be exported in several formats: gml, kml, shapefiles.

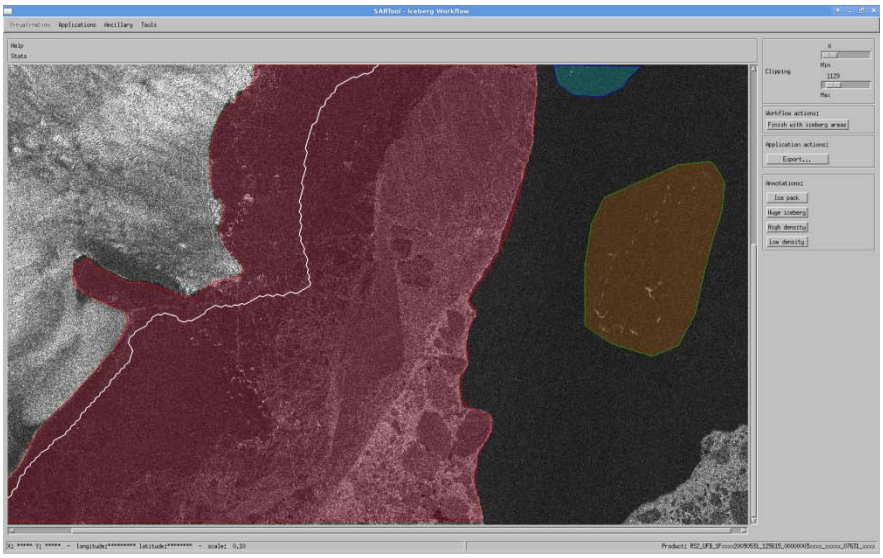

Figure 3-2 Example of SARTool annotations module used by CLS analysts for icebergs detection

3.3 Objective of this study

The detection of icebergs in the ice pack is a scientific/technical challenge. As identified in the deliverable D5.1, the CFAR based approach is not adequate for iceberg detection in the ice pack. In

addition, it may fail in the marginal zone given the strong ambiguities with pancake ice. As a consequence, high-resolution sea ice classification is strongly required to provide an a priori knowledge in order to apply the appropriate methodology for iceberg detection.
Nowadays, ice charts are manually generated by National Ice Centres (e.g. Met.No., Finnish Meteorological Institute) at kilometric scale by using not only SAR data but also a large set of ancillary information. Innovative studies should be foreseen to generate automatically this kind of high-resolution ice maps for a future integration into the iceberg detection processes.

Over the open water, the automatic CFAR-based detection should be further tuned so as to decrease the number of false alarms. This activity should be carried out for a limited number of SAR acquisition modes (e.g. dual pol HH/HV RS2 ScanSAR Wide / Narrow mode), which could be potentially used for routinely operational use.

3.4 Automatic iceberg detection

Some studies have been initialized regarding the automatic iceberg detection with medium resolution SAR images. In particular, the SIDARUS consortium can access a set of RS2 images over the Barents Sea via the ESA data warehouse mechanism. As shown in Figure 3.3, more than 200 images are available from January to April 2012. Most of these images are ScanSAR Wide images with 50 m pixel spacing and dual-polarization channels (HH and HV). In addition, a limited set of ScanSAR Narrow images (25 m pixel spacing) is also available.

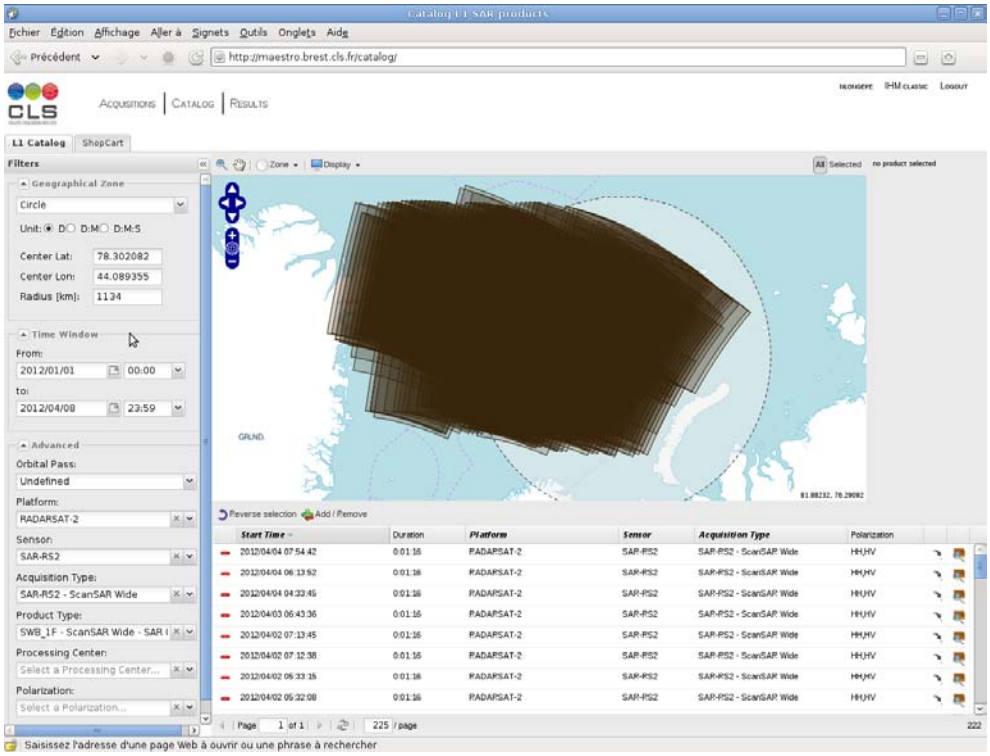

Figure 3-3 List of RS2 images in ScanSAR Wide mode available from 2012/01/01 to 2012/04/04, viewed in the Maestro web interface

(1) Automatic detection based on RS2 ScanSAR Wide images

The objective of this section is threefold:

- Run the automatic CFAR-based iceberg detection over the Barents Sea with various ice conditions (open water, marginal zone, ice pack with FYI or MYI) over a large number of SAR scenes
- Eventually tune the detection algorithm and the qualification method (reliable/unreliable)
- Compare the results with ENVISAT altimeter-based detection.

CFAR-based methodologies are based on a pre-determined false alarm rate, which is then used to compute the appropriate threshold given a probability density function for the clutter. The parameterization of the clutter distribution is carried out locally with a sliding window. The window is generally partitioned into three parts as shown by Figure 3.4. The cell under test is in the middle. Purpose of the guard area is to ensure no part of an extended target is included in the background area and hence the clutter area is representative of the background statistics.

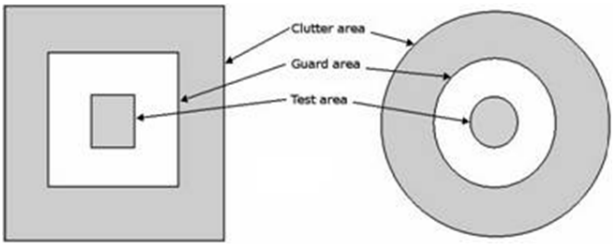

Figure 3-4 CFAR kernel

Thus, dimensions of target, guard and background areas in pixels domain have to be adapted to image resolution in both range and azimuth directions, and to the minimal and maximal dimensions of the iceberg under consideration. In the case of areas with dense iceberg fields or deformed sea ice, the clutter area may contain undesired bright targets that contaminate the statistics. As a result, CFAR-based target filter may not detect some bright echoes.

Then a rejection of false alarm corresponding to radiometric ambiguities (weak targets), azimuthal and nadir ambiguities is carried out. The remaining potential targets are then qualified as “reliable” or “unreliable”. In the current version of the SARTOOL software, the reliability of the detected echoes is computed from various parameters such as the resolution of the sensor, the Equivalent Number of Look (linked to the rate of spatial averaging), the incidence angle, the Normalized Radar Cross Section (NRCS) and a coefficient computed by the CFAR methodology (more specifically, the difference of RCS between the test and the clutter areas normalized by the standard deviation of the RCS over the clutter area). This complex rule has been originally built from a Neural Network for the application of ship detection and has been slightly tuned for icebergs. The qualification “reliable vs. unreliable” needs to be further studied and adapted for icebergs with new modes/sensors. This is especially true in the context of the end of the ENVISAT mission, and its replacement for iceberg monitoring by RS2 sensor.

The following figures show the results of the automatic detection process from HH-polarized (see Figure 3.5) and HV-polarized RS2 images (see Figure 3.6) over the Barents Sea during the period February-March 2012. Before analyzing the results in details, the following comments should be outlined:

- The automatic SAR iceberg detection has supposedly better performance over open water. In the figures, the ice concentration from AMSR-E sensor computed by the University of Bremen is used to distinguish open water from ice. The green, cyan and blue symbols indicate iceberg positions with ice concentration below 10%, between 10% and 50%, and over 50%, respectively. Given the CFAR procedure, the “green” detections can be considered as relevant as opposed to the others, which should be taken with caution.

- The ice concentration is computed with a resolution grid of 6.25 km. Near by the coast, no such information is available and the detected icebergs are plotted in orange. This kind of detected icebergs is considered as relatively relevant because ice close to the coast is relatively homogeneous and CFAR procedure has likely good performance. Land-fast ice is usually ice that has frozen along coasts or to the sea floor over shallow parts of the continental shelf. As opposed to drift ice, it does not move with currents and wind.
- In this current version, simply threshold rules based on the aforementioned "CFAR coefficient" and the NRCS of the target have been applied in order to reject the unreliable targets.

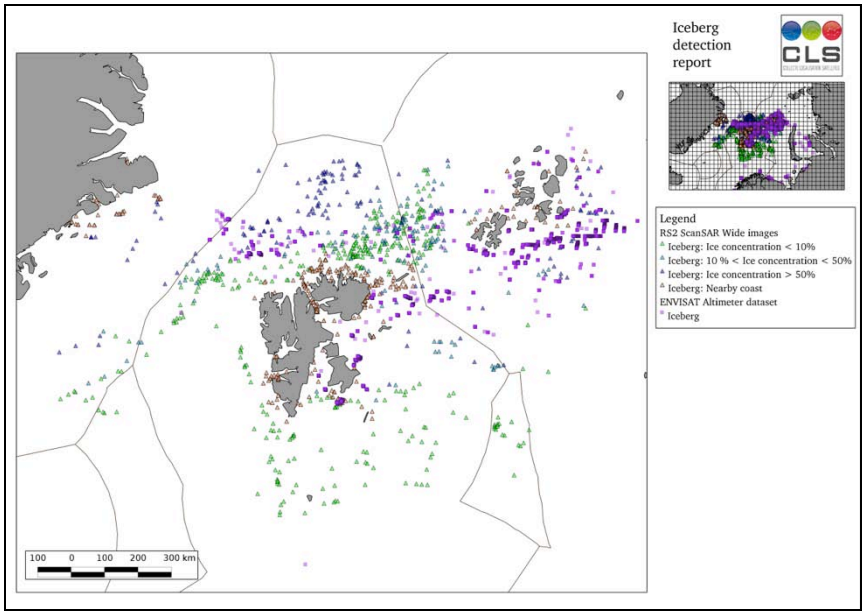

Figure 3-5 Detected icebergs in February and March 2012 from RS2 ScanSAR Wide imagery with HH polarization coupled with altimeter-based detection

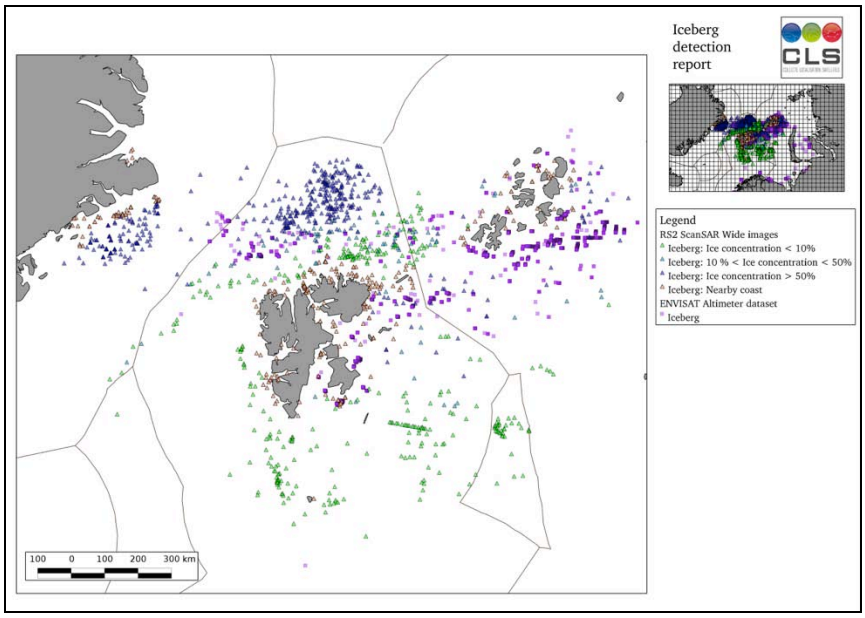

Figure 3-6 Detected icebergs in February and March 2012 from RS2 ScanSAR Wide imagery with HV polarization coupled with altimeter-based detection

From the two figures, the main conclusion is that the detections from SAR and altimeter occur over different locations. Most of the altimeter detections are located on the south of Franz-Joseph archipelagos and on the North-West of Svalbard. The SAR-based detections are sparser:

- Nearby the coast of Svalbard and in between Franz-Joseph archipelagos: as previously mentioned, these detections are supposedly quite reliable since the ice conditions are generally homogeneous in these areas.
- South and North-West of Svalbard: Most of the "green" detections are presumably vessels with a small probability of icebergs.
- Nord-East of Svalbard: these "green" detections are likely false alarms as this area corresponds to a marginal zone as seen in the figures.
- North of Svalbard with the "blue" symbols: These detections correspond to areas with MYI with a presence of large floes and deformed ice. The detections are very likely "false alarms", especially for the HV channel, which seems less robust than HH channel for bright targets detection in deformed/MYI ice.

This preliminary study will be further completed and described in the final deliverable D5.5. Especially, a new version of the detection and qualification processes is currently under development. It integrates an adaptive CFAR process using variable false alarm rate and a qualification process using a Neural Network approach.

At this stage, it should be noted that ship and iceberg detection algorithms are generally similar. Nonetheless, the ability to discriminate iceberg targets from vessel targets is of high importance in some regions. In (Howell et al. 2006), a methodology to classify these two kinds of targets is described. Based on a so called "sequential forward selection », relevant features (geometric, radiometric) are iteratively added and a multivariate classification scheme is performed finally. It is demonstrated that icebergs and ships can be discriminated with 93.5% accuracy by using HH/HV dual-polarized data. This kind of methodology could be investigated during the last year of the project.

(2) Benefit of ScanSAR narrow at 25m resolution

Dedicated acquisitions have been carried out in February 2012 in order to assess the benefit of 25 m pixel spacing data with respect to 50m. In particular, the RS2 ScanSAR narrow mode images have been ordered via MyOcean users (for instance MetNo) and made available via the ESA Datawarehouse mechanism.

In February, two images have been acquired with a 3-days interval. The analyses of iceberg detection have been performed by trained analysts in an independent manner. Results are shown in Figure 3.7.

The number of detections is quite different depending on the dataset:

- The benefit of 25m pixel spacing over 50 m is obvious: the number of "reliable" detections is much higher in the first case. Up to now, MyOcean users routinely acquire ScanSAR wide imagery (larger swath width) which is detrimental for iceberg detections. For a future evolution of the MyOcean operational service, the use of ScanSAR Narrow product is strongly recommended for the iceberg-related activities in the Arctic regions.
- With 50m pixel spacing, no "unreliable" target has been indicated by the analyst. At this resolution, this information does not seem relevant for operational use, as opposed to ScanSAR Narrow detection with many "unreliable" targets.

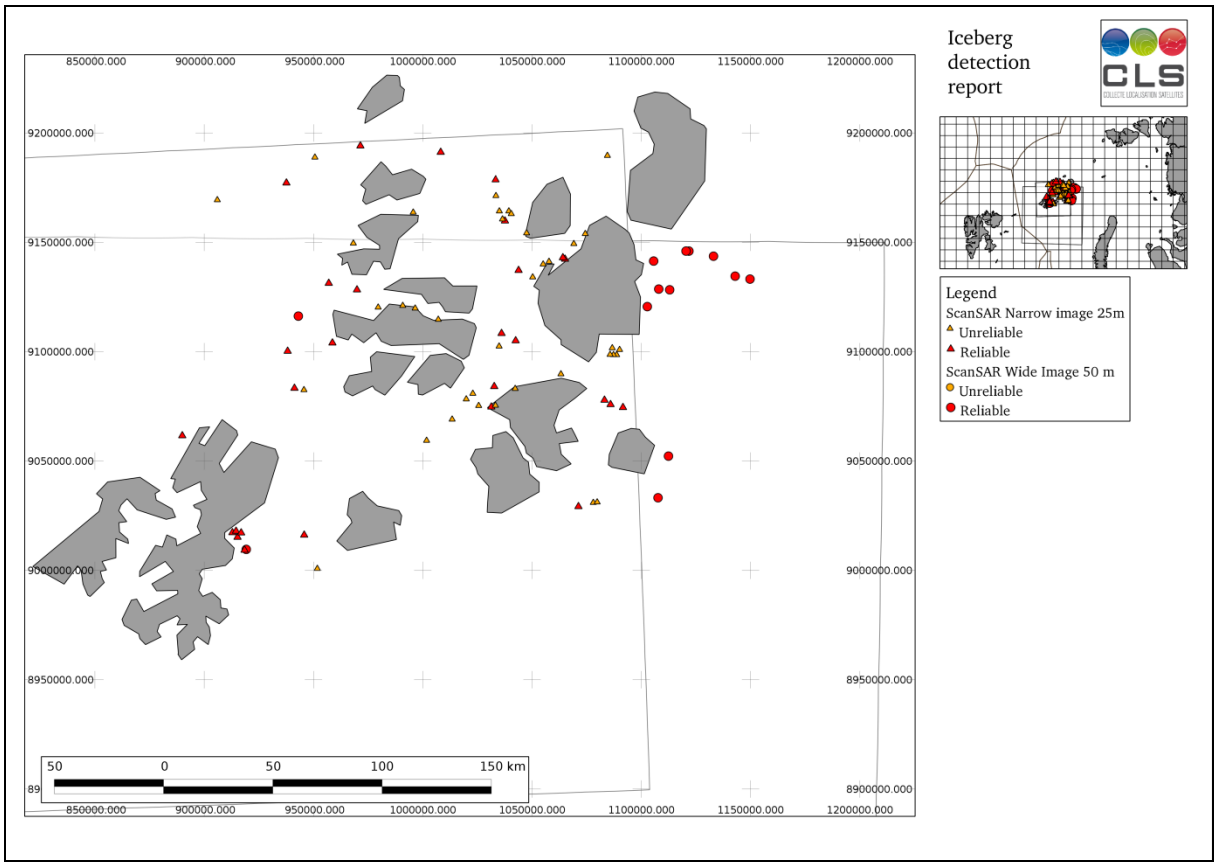

Figure 3-7 Comparison between detections carried out by using RS2 ScanSAR wide and RS2 ScanSAR Narrow images acquired in February 10 and 7, respectively

3.5 Advanced ice and iceberg segmentation

As it has been already mentioned in the deliverable D5.1, there exist different approaches for SAR-based iceberg detection (see Table 2) depending on the imaging mechanisms. The CFAR-like approach is robust for large icebergs and medium resolution SAR images. Depending on the SAR resolution relative to iceberg size, the incidence angle or the surrounding of the iceberg, no bright target appears. As a result, the CFAR approach fails in the detection. Through the SIDARUS project, CLS has initialized an innovative methodology for image segmentation in ice environment.

(1) Image Segmentation for complex Arctic environment

Image segmentation has been a very active research field for the last twenty years. SAR images are subject to a multiplicative noise, called speckle, with which a constant reflectivity area on ground corresponds to an area with strong grey level variations from pixel to pixel in the image. This makes it difficult to apply classical segmentation techniques designed for optical images. An important work has been made to process images affected by speckle noise. The requirements applicable to the selected segmentation algorithm derive from operational constraints and the particular characteristics of the images to be processed, namely:

- The algorithm shall be fully autonomous, i.e. shall not need a manual tuning of parameter, from one SAR image to the other.
- The algorithm shall be robust to speckle noise.
- Due to the variation of local incidence across the swath, the algorithm shall be robust to variations in water / ice contrast throughout the swath.

- A previous segmentation (or an eroded version of the current water mask) may be used as a starting point for the segmentation algorithm

Table 3-1 Different approaches for SAR-based iceberg detection

Imaging mechanism	**Possible detection methods**	**Comments**
Double-bounce scattering	CFAR-like approach	Commonly used method, robust, good capacities except at steep angle or strong wind condition
Shadowing	Dark point-target detection	Observable with decametric resolution only
Effect of surrounding sea surface, wakes	Dark point-target detection, Segmentation, Hough transform	Strongly depend on sea condition
Shape	Image segmentation	Large icebergs only
Volume scattering	Multifrequency or polarimetric approach	Observable only with multi channel data, only for open water

Different algorithms have been investigated:

- The first approach was to apply speckle reduction filters prior to classical segmentation techniques such as multi-modal thresholding based on histograms (Lee 88). The main drawback of this approach was the degradation of the spatial resolution due to the smoothing of contours. Nevertheless this approach could be revisited since promising speckle filtering techniques have recently been published.
- To overcome the resolution issue inherent to speckle noise reduction, edge-based detectors were designed so as to detect transitions between uniform regions rather than directly identify them. In the framework of statistical decision theory, (Oliver et al. 1995) determined an optimal filter, based on the likelihood ratio (LR) principle. However, it has been shown in (Germain et al. 2000) that these edge-based detectors introduce a bias and increase the variance in the estimation of the edge position when the window has not the same orientation as the edge (which is a practical situation since the edges may have arbitrary orientation in the image).
- Other approaches such as region growing or region merging have also been developed. In particular the MUM (Merge Using Moments) technique introduced by (Cook et al. 1994) which starts with an over-segmentation of the image and applies a scheme based on examination of the statistical properties (moments) of adjoining regions to decide when to merge them and produce a coarser and more adequate segmentation. This scheme is employed iteratively until no remaining merge appears valid, at which time a good segmentation is obtained.

- Because they permit to take into account the noise model, Bayesian image segmentation techniques have become more and more attractive since the work of (Geman and Geman 1984) on making an analogy between images and mechanical systems in the sense of statistical mechanics. In this approach the pixel grey levels and the presence and orientation of edges are viewed as states of atoms or molecules in a lattice, like physical system, so that for a range of degradation processes, such as multiplicative or additive noise, the posterior distribution is a Markov Random Field. The main drawback of these techniques is that they introduce some new parameters to be selected. Bayesian techniques based on Markov random fields exhibit many interesting properties.
- A large interest has been devoted to variational methods for image segmentation with an Active Contours (AC) or Snake in a 1 pixel-thick curve indexed by time defined within an image domain: C = { x(t) ; y(t) }, t being the curvilinear index. The authors of the first paper on AC (Kass et al. 1988) also named it "Snakes" because of its movements under the influence of internal forces coming from within the curve itself, external forces computed from the image data and interaction forces between internal and external forces.
- In a recent paper (Galland et al. 2003) and in the frame of a PhD thesis (Galland 2004) a new minimum description length (MDL) approach was presented based on a deformable partition (a polygonal grid) for automatic segmentation of speckled image composed of several homogeneous regions. The image segmentation thus consists in the estimation of the polygonal grid, or, more precisely, its number of regions, its number of nodes and the location of its nodes. These estimations are performed by minimizing a unique MDL criterion, which takes into account the probabilistic properties of speckle fluctuations and a measure of the stochastic complexity of the polygonal grid. This approach then leads to a global MDL criterion without undetermined parameter since no other regularization term than the stochastic complexity of the polygonal grid is necessary and noise parameters can be estimated with maximum likelihood-like approaches. The performance of this technique is illustrated on synthetic and real Synthetic Aperture Radar images of agricultural regions and the influence of different terms of the model is analyzed. The same technique has been used for oil spill segmentation (Galland et al. 2004).

The outcome of the bibliographic study is that few techniques seem to be in position to perform automatic segmentation of medium resolution SAR images into an a priori unknown number of regions with no parameter tuning and no initial contour. One method in particular, namely the MDL polygonal grid, seems to offer a robust and fully autonomous solution.

(2) The MDL polygonal grid segmentation for complex Arctic environment

The implementation of this segmentation scheme has been initialized. Its main advantages are the optimization of a unique and parameter-free criterion through a simple and intuitive approach. A minor drawback is that this is a parametric statistical method based on the assumption of a gamma law of either a fixed order or an order that needs to be estimated. Moreover its precise implementation is subject to some choices and requires a complex optimization scheme, which is not sufficiently detailed in the literature. This deliverable D5.3 is not aimed at being a comprehensive Algorithm Theoretical Breakdown Document; we will just briefly describe the algorithm and comment the performance of our draft implementation of it

(3) Algorithm

An initial arbitrary partition of the image is built using a grid that defines regions based on nodes and segments. The nodes, which are the junction of 2 or more segments may be moved in 8 major directions and may be deleted when they interconnect only 2 segments. The segments, which separate neighbor regions need to be recomputed when a node is moved, they may also be deleted

to merge 2 regions together. The segments that define the border of the image can neither be moved nor be deleted but the border segments from 2 merged regions maybe replaced by a unique segment after deletion of their interconnecting node.

The algorithm iteratively scans the grid and tries any of following the 3 steps:

- Region merge
- Node displacement
- Node deletion

to minimize the description of the image in terms of number of regions, number of segments and nodes as well as homogeneity of the regions through the description of their statistical content.
To evaluate the complexity of the image description with regions, segments, nodes and statistical law parameters, a unique criterion is evaluated: the Stochastic Complexity. This criterion involves:

- The geometrical partition code length (the entropy of the code length of the message that describes the topology of the grid)
- The statistical parameters code length (the entropy of the statistical parameters and the number of pixels that define each region)
- The data entropy computed from the pixels when grouped into regions defined by the above statistical parameters.

(4) Performances

Our implementation of the algorithm does the job quite well as depicted on the partitioned images below but suffers from several drawbacks that would need important efforts to be solved:

- It is extremely slow since interpreted language like IDL is not appropriate to this kind of algorithm (conditional algorithm). The software module should be transposed into a more appropriate language with serious parallelization capabilities.

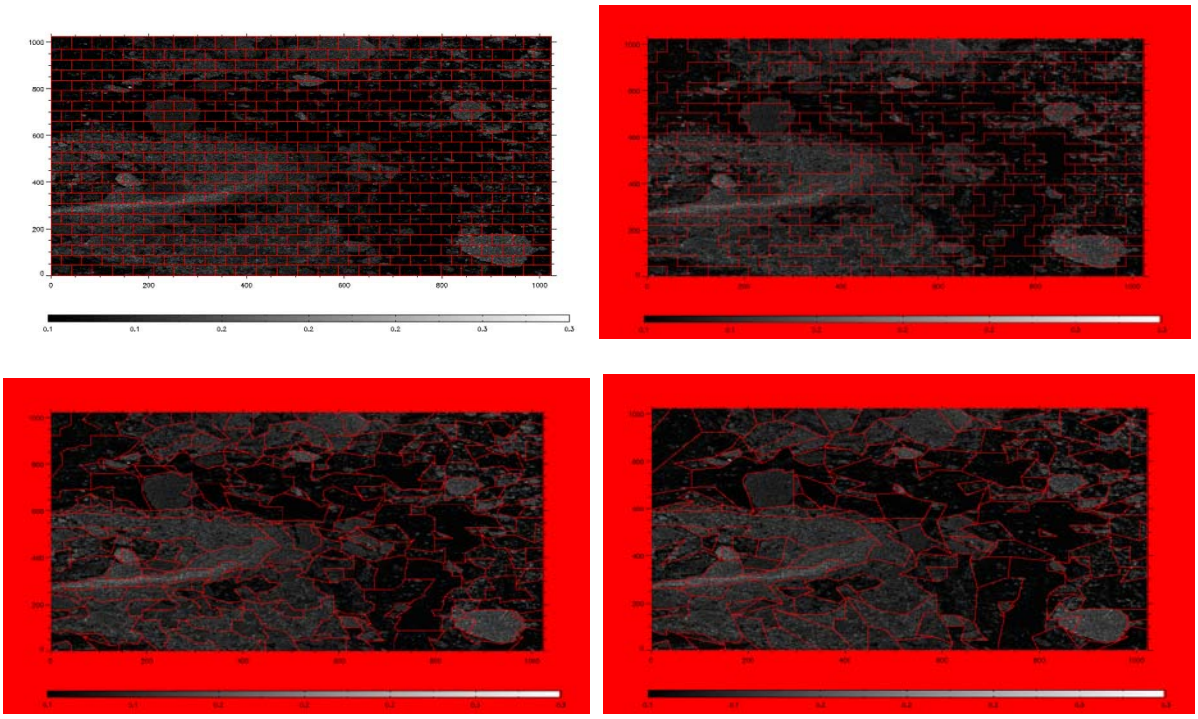

Figure 3-8 First segmentation result using a MDL polygonal grid approach of a WSM ASAR image with sea ice, iceberg and ice floes. (Top – Left): initial grid (Bottom – Right): segmentation after 4 iterations (nodes merge/move/delete)

- Numerous temporary objects are created when testing the various hypotheses (for example the move of nodes in different directions implies the creation of temporary segments and regions and the re-computation of their temporary statistics): a better handling should be made.
- An optimized scanning of the grid should be implemented taking into account the last modification of the grid to drastically reduce the number of tests for the future evolution of the grid.
- Despite the efforts already made to avoid segments' cross-over and regions' intersection when moving or deleting nodes and reconnecting the neighbors nodes together, a thorough check of the topology handling should be made.

3.6 Conclusions

From the first results obtained with this algorithm we are already convinced that it has a great potential to solve our ice segmentation issues if the proposed corrective actions are performed. Because of its capacity to automatically segment an image perturbated by speckle noise into an unconstrained number of regions with very little a priori information (the gamma law), it is a very sound basis for a robust classification (region per region and not pixel by pixel).

References

R. Cook and I. Mc Connell, "MUM (merge using moments) segmentation for SAR images" in Conf. on SAR Data Processing for Remote Sensing, Rome, Italy. SPIE, 1994, vol. 2316, pp. 92-103.

F. Galland, .Partition d.images par minimisation de la complexité stochastique et grille active: application à la segmentation d.images de radar à ouverture synthétique", Thèse de doctorat,Univ. Aix Marseille III, 2004.

F. Galland, N Bertaux, P Réfrégier, .Minimum description length synthetic aperture radar image segmentation,.IEEE Transactions on Image Processing, vol. 12, p. 2003.

F. Galland, P. Refregier, et O. Germain, .Synthetic Aperture Radar oil spill segmentation by stochastic complexity minimization,.IEEE Geoscience and Remote Sensing Letters, vol. 1, 2004, p. 295.299.

S. Geman et D. Geman, .Stochastic Relaxation, Gibbs Distribution, and the Bayesian Restoration of Images,.IEEE Transactions on Pattern Analysis and Machine Intelligence, vol. 6, pp. 721-741, 1984.

O. Germain and Ph. Réfrégier, "On the bias of the Likelihood Ratio edge detector for SAR images", IEEE Trans. Geoscience and Remote Sensing, vol. 38, no. 3, pp. 1455-1458, 2000.

Howell C., Jason Mills, Desmond Power, James Youden, Kelley Dodge, Charles Randell, and Stephen Churchill, Dean Flett, "A Multivariate Approach to Iceberg and Ship Classification in HH/HV ASAR Data". IEEE Geoscience and Remote Sensing Symposium, 2006

M. Kass, A.Witkin, and D. Terzopoulos, "Snakes: Active contour models", International Journal of Computer Vision, vol. 1, pp. 321-331, 1988.

J. Lee, Jurkevich, Segmentation of SAR images, IGARSS 1988.

N. Longépé, F. Mercier, J.Y Lebras, M. Sutton, G. Hajduch, “Iceberg monitoring service by joint use of drift model, SAR and altimeter data”, SeaSAR symposium, June 2012

C. J. Oliver, I. Mc Connell, D. Blacknell, and R. G. White, "Optimum edge detection in SAR" in book "Synthetic Aperture Radar and Passive Microwave Imaging", G. Franceschetti, C. J. Oliver, l.C. Shiue , and S. Tajbakhsh , Eds 1995 , vol 2 58 4 , pp. 152-163

4 Tracking of sea ice motion

S. Linow and W. Dierking, AWI

4.1 Introduction

Sea ice motion can be estimated from a set of two radar images recorded at different points in time. Here, we focus on a pattern-tracking approach to determine the displacement of structures in the sea ice. In the following sections 4.2 and 4.3, we describe the image preprocessing steps and the functioning of the algorithm. For a demonstration of the application of our algorithm, we use an example dataset acquired over the Weddel Sea. The test site was chosen to cover the Ronne Polynia (Figure 4.a). Coastal polynias are regions where catabatic winds from the ice shelf move the sea ice away from the coast and where, as a consequence, new ice is formed.

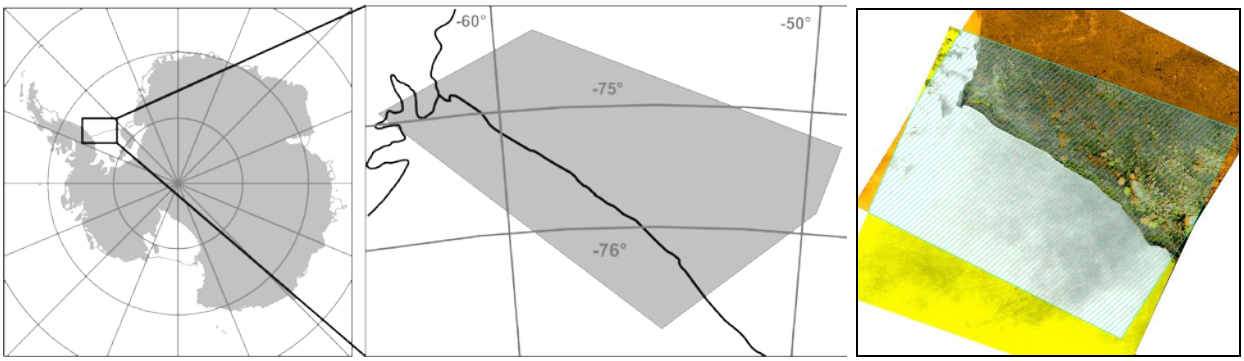

(a) (b)

Figure 4-1(a) Drift algorithm test site, (b) overlapping image region (hatched) of SAR images recorded on 18.02.2008 (orange) and 19.02.2008 (yellow)

For our algorithm, this implies some interesting test cases. First, there is the shelf ice region which is static for the time span of our observations as well as more or less featureless. Our test images also include regions of older pack ice with stable structures which are relatively easy to track visually. Then, there is the polynia region where patterns in the ice are very dynamic. Our test data are Envisat ASAR Wide Swath images acquired in February/May 2008. A further test of the algorithm was carried out in collaboration with the Norwegian Meteorological Institute. For this test, we used Radarsat-2 images from September 2012 acquired over Fram Strait. Results from our test sites are shown in section 4.4.

4.2 Image preprocessing

As a first step, the radar images are radiometrically calibrated and geocoded using the ENVI/Sarscape software package. For speckle reduction, the SAR data are resampled to a spatial resolution of 150x150m in the case of Envisat Wide Swath images, and to 100x100m in the case of Radarsat-2 ScanSAR images. Subsequently, an enhanced Lee filter is applied. Next, the overlapping regions of

the image pair are cut out (Figure 4.1b). The result of these preprocessing steps is an image pair containing the overlapping region of both images and some metadata which are needed later to restore the geolocation information. The algorithm reads all required information from a file:

- Number of cascade steps (see section 4.3)
- Depth of the resolution pyramid (see section 4.3)
- Names and paths of the input file pair
- The name of a file containing reference drift data for algorithm validation
- A flag for using the reference data
- A flag for using histogram equalization

In some cases we manually determined a set of drift vectors for later validation of the result.

4.3 The ice drift algorithm

(1) Cascaded motion tracking

Sea ice drift is estimated using a pattern-based cascaded motion tracking algorithm initially developed by Thomas [2008] and adapted by Hollands [2012]. The algorithm iteratively calculates the displacement field as follows.

At the beginning, a resolution pyramid is generated from the input images. In a first step of the displacement calculation, a low-resolution motion field is estimated from a low-resolution set of images, serving as a first guess for the drift estimate (Figure 4.2a). The pattern matching routine requires a region of each image where it can search for corresponding patterns. This region is called search window or template.

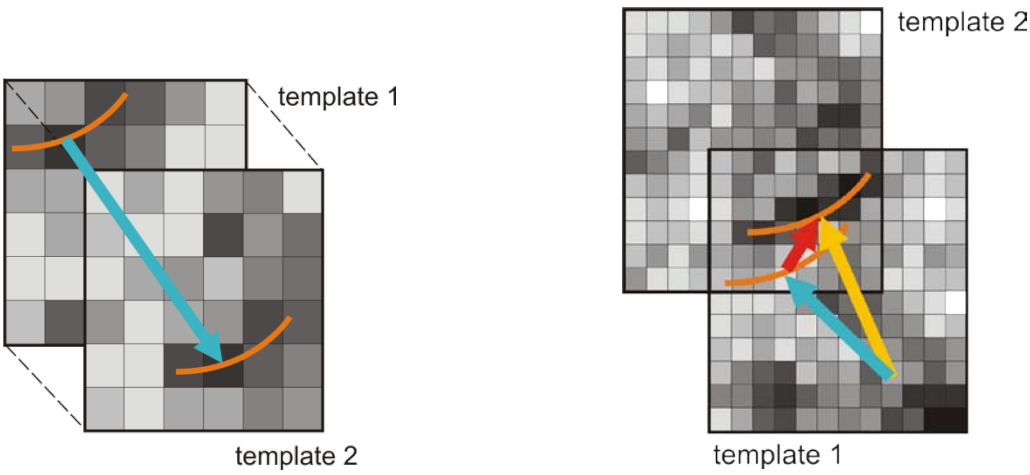

(a) (b)

Figure 4-2 (a) displacement field initialization, (b) refined displacement calculation. (Note that order of images is reversed).

The next step uses a refined resolution of the image pair to analyze more detailed patterns. The example in Figure 4.2b shows the same template as Figure 4.2a, with twice the image resolution. At each step in the resolution pyramid, the displacement field is initialized using the field estimated during the previous step, and the algorithm searches in a predefined direction. In our example, we shift the template from image 2 by the displacement shown in Figure 4.2a, indicated by the blue arrow (corresponding to the arrow in Figure 4.2a). The red arrow in Figure 4.2b indicates the incremental displacement calculated during this step and the yellow arrow shows the total estimated displacement.

The refined displacement is calculated incrementally in this way during the following steps, until the highest image resolution is reached. Then, the resolution of the displacement field is doubled and initialized with the results from the previous cascade step. The refined displacement field is again iterated over the image pyramid, and those steps are repeated until the highest resolution of both the image pair and the displacement field are reached. The entire procedure is sketched in Figure 4.3.

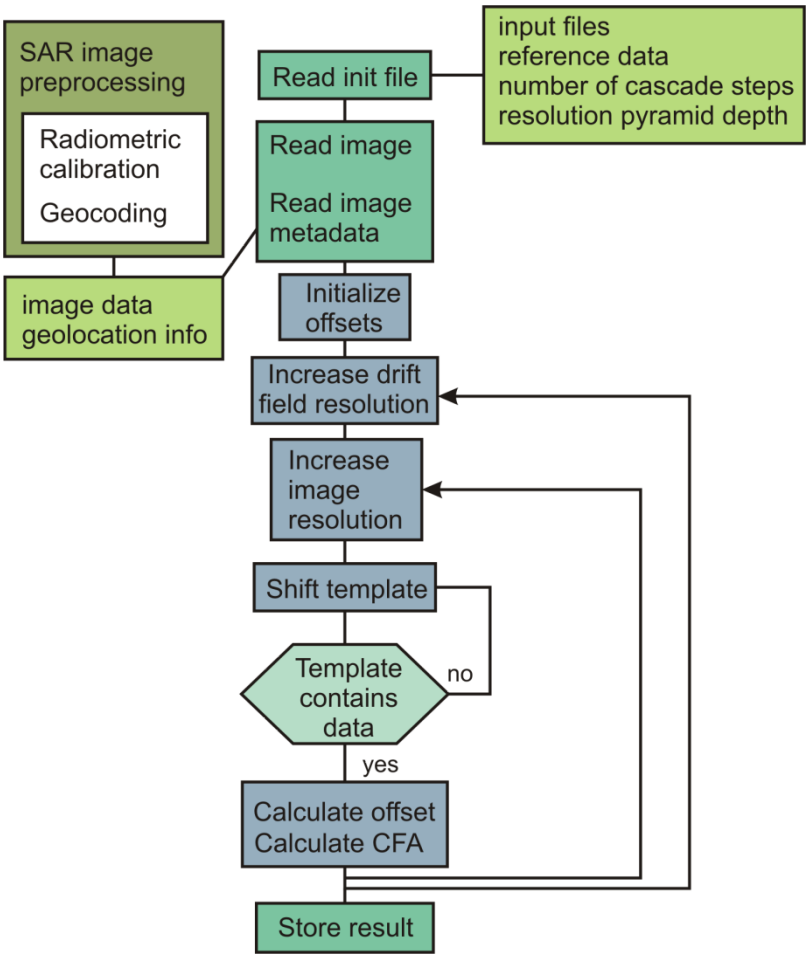

Figure 4-3 Drift field calculation flowchart

(2) Pattern matching

The actual pattern matching combines two different methods: a phase correlation approach to identify patterns in the Fourier domain, and the calculation of the normalized cross-correlation coefficient to select the best match.

$$PC(u,v) = F^{-1}\left[\frac{F(h)\cdot F^{*}(g)}{\left|F(h)\cdot F^{*}(g)\right|}\right] \tag{4.2}$$

The phase correlation (PC) approach, as shown in equation (4.2), was adapted from Canty [2007]. *PC* is the normalized cross-power spectrum calculated from the Fourier transform *F(h)* of the image template *h* from the second image shifted by (*u,v*) and the complex conjugate of the Fourier transform $F^{*}(g)$ of template *g* from the first image. The phase correlation has been found to be quite robust in the presence of variations of illumination or offsets in the average image intensity [Foroosh et al, 2002], but on the other hand it is sensitive to additive high-frequency noise [Eckstein and Vlachos, 2009; Manduchi and Mian, 1993].

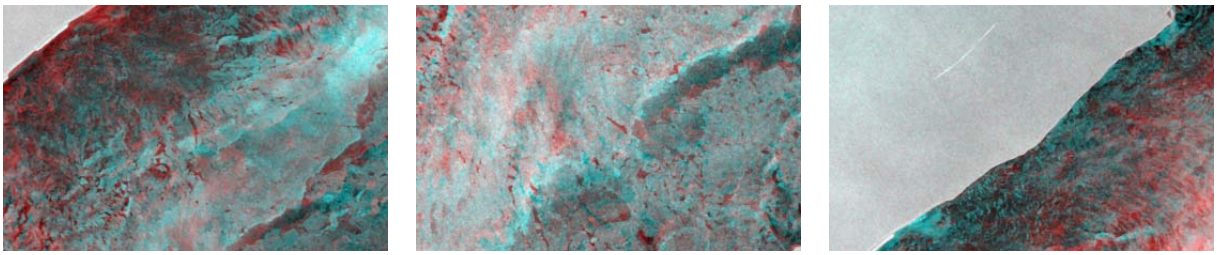

(a) (b)

Figure 4-4 Superposition of two image zoom-ins, g (red) and h (cyan) for (a) polynia and ice shelf, (b) pack ice, (c) ice shelf. Displacements in the sea ice can be recognized.

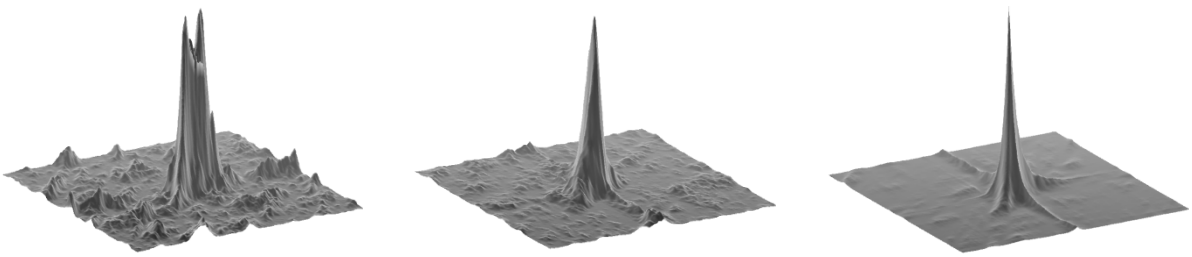

(a) (b) (c)

Figure 4-5 Example phase correlation functions for (a) polynia and ice shelf, (b) pack ice, (c) ice shelf

In the ideal case, the phase correlation displays a sharp peak at the position of the spatial offset of both templates, as for instance in Figure 4.5c. In this special case, the peak is caused by the prominent structure of the shelf ice margin (Figure 4.4c). A typical example of a phase correlation caused by patterns in the sea ice is shown in Figure 4.6b and Figure 4.5b. Under certain conditions, the phase correlation function can display multiple maxima (Figure 4.4a). In our example, this is caused by the static shelf ice edge and the actual drifting sea ice patterns in the image templates (Figure 4.4a). To avoid ambiguities caused by the presence of multiple maxima in the phase

correlation function, we follow the approach introduced by Thomas [2008] and estimate the "correct" displacement using a normalized cross-correlation coefficient (*NCC*, equation (4.3)) for a set of displacement candidates.

$$NCC_{x,y}(u,v) = \frac{\sum_{j,k=0}^{N}[h_{u,v}(x_k,y_j)-\bar{h}_{u,v}]\cdot[g(x_k,y_j)-\bar{g}]}{\sqrt{\sum_{j,k=0}^{N}[h_{u,v}(x_k,y_j)-\bar{h}_{u,v}]^2\cdot[g(x_k,y_j)-\bar{g}]^2}} \tag{4.3}$$

Here, $\bar{h}$ and $\bar{g}$ are the mean intensities of the templates *h* and *g*, respectively. The candidates for *NCC* calculation are the largest 25% of the PC peaks. By combining both approaches, a more stable result can be achieved since the *NCC* is more robust in the presence of noise [Lewis, 1995]. Since it cannot be calculated in the spatial domain, it is numerically less efficient than the phase correlation.

Ambiguities such as shown in our example can occur in the case of high-resolution templates covering large image areas. They can introduce systematic errors into the resulting drift pattern, so the quality of the results would be improved by selecting smaller templates. Unfortunately, in those cases it can happen that there is not enough texture available to track. Since the structure of sea ice can be very variable, it is difficult to estimate an optimal template size. For this reason the different resolution steps are necessary to obtain a robust estimate for the displacement vectors.

It can still happen that spurious displacement vectors appear at each resolution or cascade step due to false pattern matches. We assume drift patterns to be smooth in the sense that neighboring drift vectors have similar directions and magnitudes. Under this assumption, we remove outliers using a median filter after each iteration. Using the same assumption, we fill small gaps in the drift field caused by pattern loss within the template. The resulting displacement field estimated using this procedure has a resolution of approximately 1/10th of the original SAR image resolution, depending on the initial settings. In the case of Envisat Wide Swath data, the pixel size is 1.5 km, and for the Radarsat-2 data, the resolution of the derived displacement field is 1 km.

(3) Deformation

We can estimate the deformation of sea ice from the resulting velocity field [Leppäranta, 2011]. Here, the velocity gradient tensor *u* is decomposed into strain rate tensor $\dot{\varepsilon}$ and vorticity tensor $\dot{\omega}$:

$$u = \dot{\varepsilon} + \dot{\omega} = \begin{pmatrix} \frac{\partial u}{\partial x} & \frac{\partial u}{\partial y} \\ \frac{\partial u}{\partial x} & \frac{\partial v}{\partial y} \end{pmatrix}$$

The first invariant of $\dot{\varepsilon}$ is the velocity divergence *d*, which can be interpreted as the strain rate along the *x* and *y* axes:

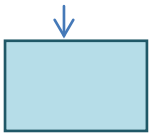

$$d = \frac{\partial u}{\partial x} + \frac{\partial v}{\partial y}$$

The second invariant is the shear *s*, it contains the off-diagonal elements of $\dot{\varepsilon}$:

$$s = \sqrt{\left(\frac{\partial u}{\partial x} - \frac{\partial v}{\partial y}\right)^2 + \left(\frac{\partial u}{\partial y} + \frac{\partial v}{\partial x}\right)^2}$$

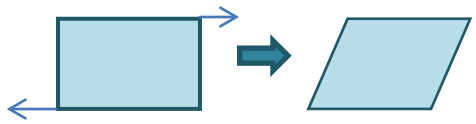

Rotation of the velocity field can be caused by different velocities acting on the field element. This is described by the invariant of $\dot{\omega}$, the vorticity *v*:

$$v = \frac{\partial v}{\partial x} - \frac{\partial u}{\partial y}$$

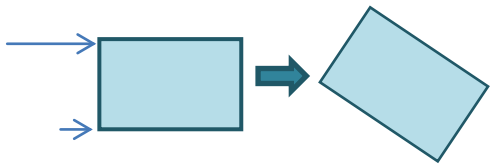

Total deformation is defined as $\tau = \sqrt{2} \cdot |\dot{\varepsilon}|$:

$$\tau = \sqrt{\underbrace{\left(\frac{\partial u}{\partial x} - \frac{\partial v}{\partial y}\right)^2 + \left(\frac{\partial u}{\partial y} + \frac{\partial v}{\partial x}\right)^2}_{s^2} + \underbrace{\left(\frac{\partial u}{\partial x} + \frac{\partial v}{\partial y}\right)^2}_{d^2}}$$

Parameters derived from the velocity field contain only information about deformation processes taking place in the time between image acquisitions. It is not possible to make assumptions of the general deformation state of the sea ice based on the derived data.

(4) Quality assessment

Displacement errors can have different sources, such as

- insufficient backscatter patterns in the radar images, which can be sometimes found in relatively featureless new ice areas
- pattern mismatches caused by a highly dynamic ice structure (areas of deformation or new ice production in polynias)
- pattern loss at the image borders
- spurious displacement vectors occuring if the search windows contain only noise
- a false initial displacement causing the algorithm to search in the wrong direction

An example of the error distribution of the derived displacement field is shown in Figure 4.6. The errors Δx and Δy were derived by subtracting manually determined displacements from the estimated velocity field. It can be seen that most errors are on the order of a few hundred meters (corresponding to approximately 2-3 image pixels). We estimate the accuracy of the manually determined displacements to be on the same order of magnitude.

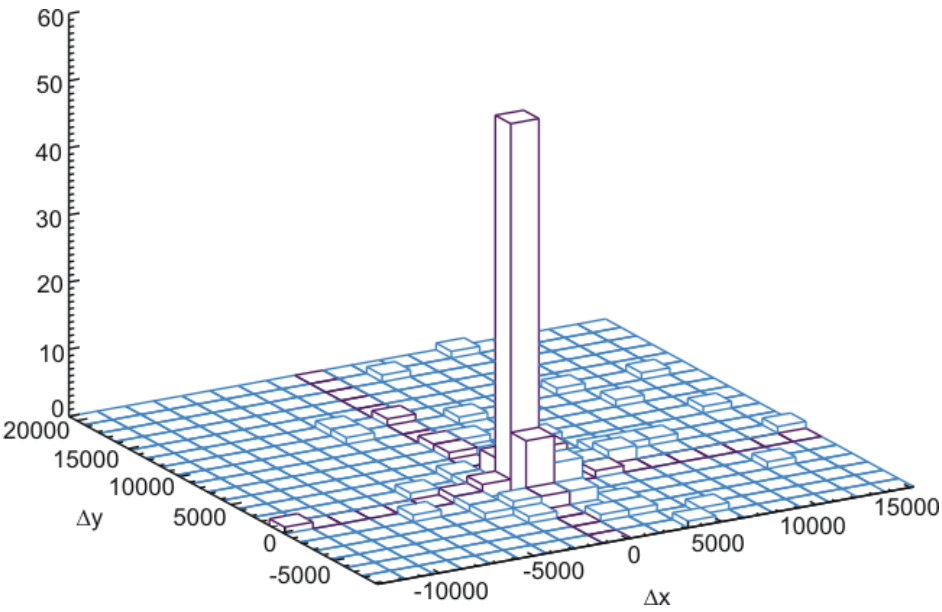

Figure 4-6 Error distribution of image pair 18./19.09.2012. Units are (m)

A quantitative analysis of the derived drift product cannot be conducted based on the correlation coefficient alone [Hollands et al., manuscript in preparation]. Therefore, the reliability of the displacement field is estimated from a combination of six different statistical and texture-based parameters. For each iteration of the displacement field calculation, those parameters are evaluated for each template pair. We then have a set of statistical measures to accompany every displacement vector.

The most intuitive procedure would be to directly exclude displacement vectors based on those statistics, but we found that this decreases the quality of the resulting displacement field, since too many vales are excluded during runtime. Instead, we set a threshold based on empirical observations for each of the six parameters. If this threshold is exceeded, we increment a counter value for the corresponding displacement vector. The counter is then, together with the displacement, inherited by the next iteration step.

At the end of the displacement field calculation, we have an error score for each displacement vector. This score needs to be normalized by the number of displacement vector iteration steps, since those are not evenly distributed (for instance, at the image margins, the number of iteration steps is lower than in the center of the image). The resulting normalized error score, or confidence factor (CFA). The following parameters contribute to the CFA:

- the *variance-to-mean ratio* (VMR) can be used to evaluate if the variance of the image brightness within a template exceeds the level expected due to speckle [Kwok, 1990]. The CFA is incremented for VMR values lower than 0.45.
- the *mean intensity gradient* (MIG) detects local gradients and returns large values if the template contains pronounced texture and low values in homogeneous regions [Pan, 2010]. We set the threshold to 1.5 for this parameter and increment the CFA if it is lower.

- the *mean gradient slope* (MGS) is another texture parameter which shows changes of the gradient map (2nd derivative) and serves as an additional hint for the occurrence of structures within the template window [Pearlstine, 2005]. We increment the CFA if MGS is < 7.
- the *normalized cross-correlation* (NCC) is used to determine the displacement between the templates, and while it cannot be used as a reliability indicator on its own, it still gives information on the quality of the pattern match. We increment the CFA if the NCC falls below 0.2
- If the number of samples in the template becomes too small, the correlation coefficient becomes unreliable . [Fily and Rothrock, 1987]. For this reason, we determine a *confidence interval* for the NCC. We increment the CFA if the confidence interval is larger than 10% of the range of NCC values.
- an *intensity threshold* of -3dB was introduced to avoid possible false matches caused by randomly occurring specular reflections [Jenkin, 1991; Shavit, 2007]

An example for the resulting CFA score is shown in Figure 4.7a. We can discern different regions. The ice shelf has large CFA values because of the lack of texture, and the image borders score high due to low correlation and correlation confidence values. At the center of the image the CFA assumes low values, as there is sufficient texture available. The polynia region scores low in our example because the CFA only checks if there is any texture available, but does not contain any information about e.g. pattern stability.

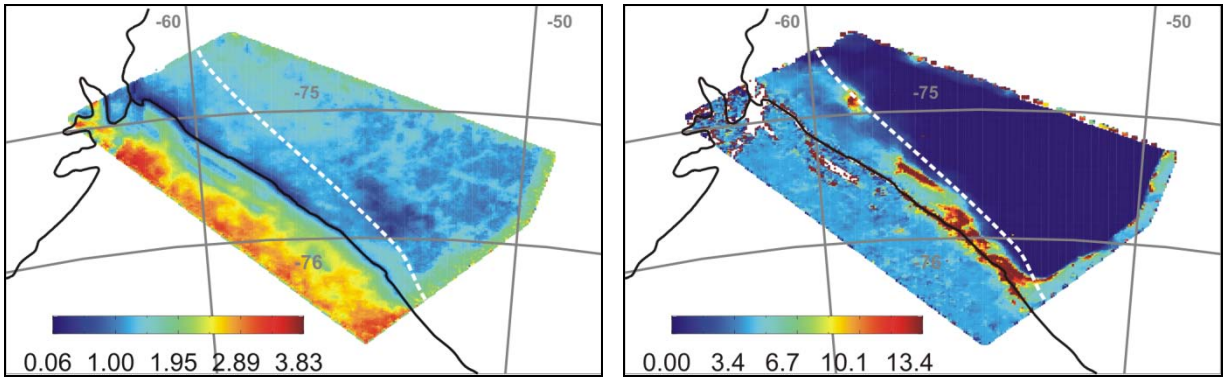

(a) (b)

Figure 4-7 Quality maps for an image pair of the Ronne polynia. (a) CFA, (b) backmatching result

Another way to validate the quality of the motion tracking result in the absence of reference data is a simple consistency check called backmatching [e.g. Schreer, 2005]. Here, the displacement field is calculated twice, with an interchanged image sequence. In regions where the algorithm makes “bad guesses” due to insufficient texture, the results from both runs are inconsistent. An example is shown in Figure 4.7b. Here, we can identify several different regions where problems can occur:

- the homogeneous ice shelf, where it can happen that only noise is correlated and all calculated displacements are rather random
- the polynia region, where the patterns are not stable enough in the time between image acquisitions

- the image borders, where patterns get lost because they drift into or out of the image

4.4 Results

(1) Ronne Polynia

In Figure 4.9a, we plot the absolute difference of the displacement vectors from backmatching over the CFA for each displacement vector estimated from the image pair recorded on the 18./19.02.2008.

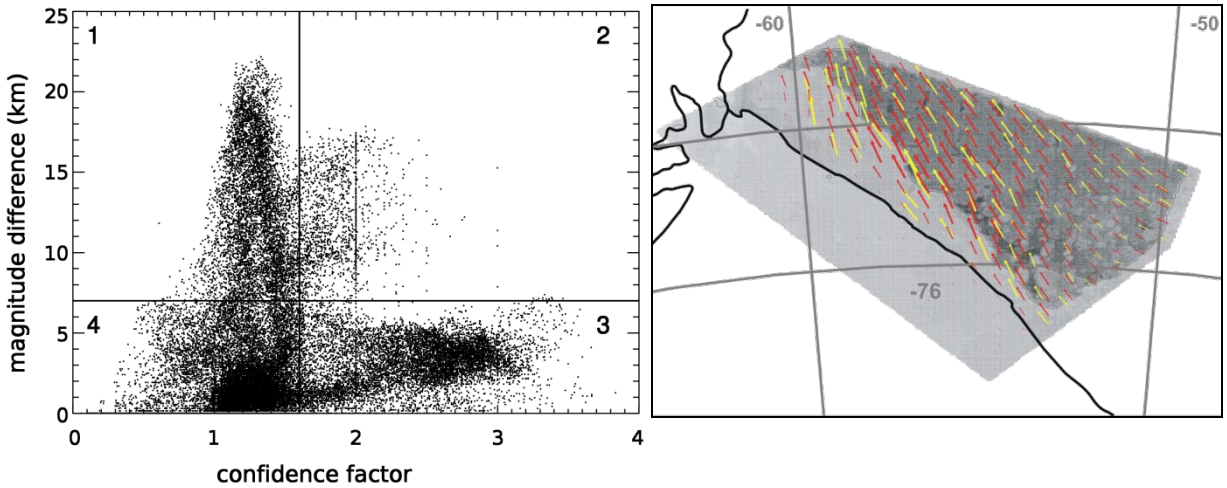

(a) (b)

Figure 4-8 : (a) scatter plot of CFA vs. backmatching difference, (b) ice drift product derived from Envisat ASAR Wide Swath image pair acquired on the 18./19.02.2008

In Figure 4.7, we can discern distinctive clusters (numbered from 1 to 4):

1. The difference from backmatching is large, but the CFA score is low. This results from a region containing sufficient texture but which changes rapidly between image acquisitions. In our example, this is the polynia region.
2. Here, both CFA score and backmatching distance are high. This cluster contains mostly values from the image margins.
3. This cluster shows a small backmatching difference, but large CFA scores, which hints to a region with low texture. In our example, this is the ice shelf.
4. The last cluster contains displacement vectors with low CFA scores which have consistent results from backmatching. We can assume that displacement vectors located in this area are reliable.

From the example shown in Figure 4.8a and the other data sets available to us, we have empirically determined a threshold for the CFA. If the CFA < 1.7, we assume the displacement vectors to be reliable. Figure 4.8b shows the displacement field obtained from our example data set. The red arrows are calculated displacements, yellow arrows represent the visually determined displacement vectors. The light grey areas correspond to classes 1-3 in Figure 4.8b.

(2) Fram Strait

Figure 4.9 shows displacement fields calculated from a Radarsat-2 image pair recorded on the 16.09.2012 with≈10h time difference between image acquisitions. Figure 4.9a shows the displacement field estimated from HH-polarization, and Figure 4.9b shows the result from the HV-polarized data. The red arrows are the calculated displacements, yellow arrows mark reference data manually derived from the image pair (in this example re-gridded to the positions of the calculated vectors). The light areas are considered unreliable from a combination of CFA and backmatching.

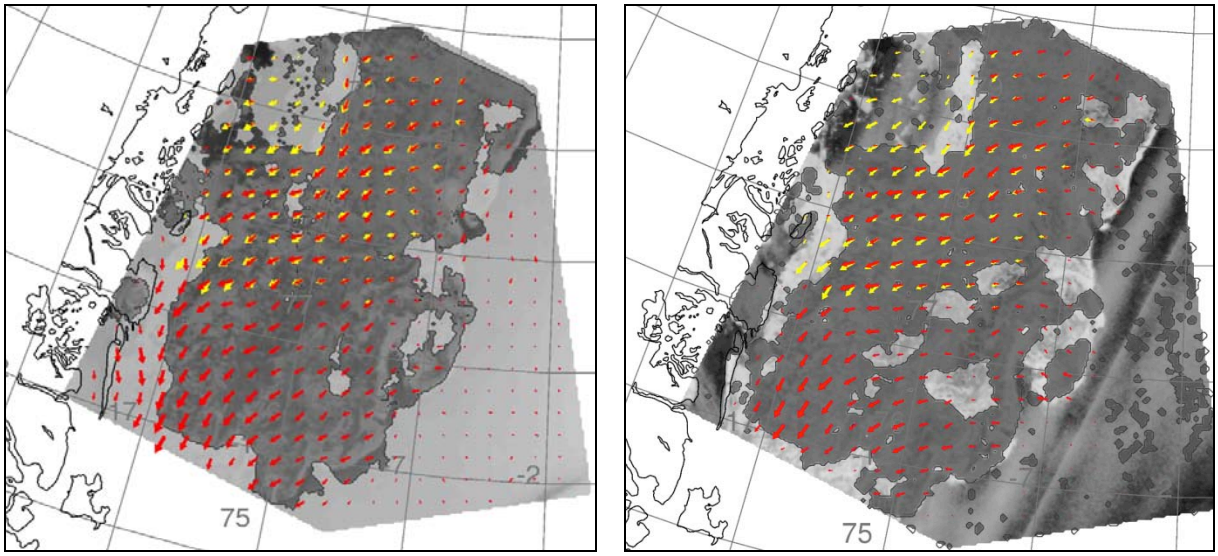

(a) (b)

Figure 4-9: Ice drift products derived from an image pair recorded on the 16.09.2012. (a) HH-polarized image pair, (b) HV-polarized image pair

It can be seen that there are slightly different regions marked as reliable, depending on polarization. The displacement field calculated from HH-polarized SAR images shows fewer gaps than the result obtained from cross-polarized data. It has been indicated that both channels are sensitive to different structures in the ice and hence contain complementary information [Komarov, 2012]. Figure **4.10**c shows an ice drift map calculated from images acquired on the 18th and 19th of September 2012, with a temporal separation of ≈24 hours. This image pair can serve as an example of the problems caused by a very dynamic ice situation. Figure 4.10a and Figure 4.10b show excerpts from two ice class charts from the Norwegian Meteorological Institute for the days of the image acquisitions. It can be seen that in the lower half of the image the ice classes change rapidly from “close drift ice” (orange) to “open drift ice” (yellow) and “very open drift ice” (green). Ice classes in the upper half of the charts stay relatively stable. The rapid change of the ice properties between the images made it difficult to visually determine reference data for the southern part of the image pair. Nevertheless, the drift direction in this area is correctly determined by the algorithm.

Figure 4.11a shows a map of the divergence calculated from the displacement field (see also section 4.3). Here, red are zones of divergence, blue zones are convergent regions. In Figure 4.11b, the vorticity of the derived velocity field is depicted. Red areas rotate in anticlockwise direction, while blue areas rotate clockwise.

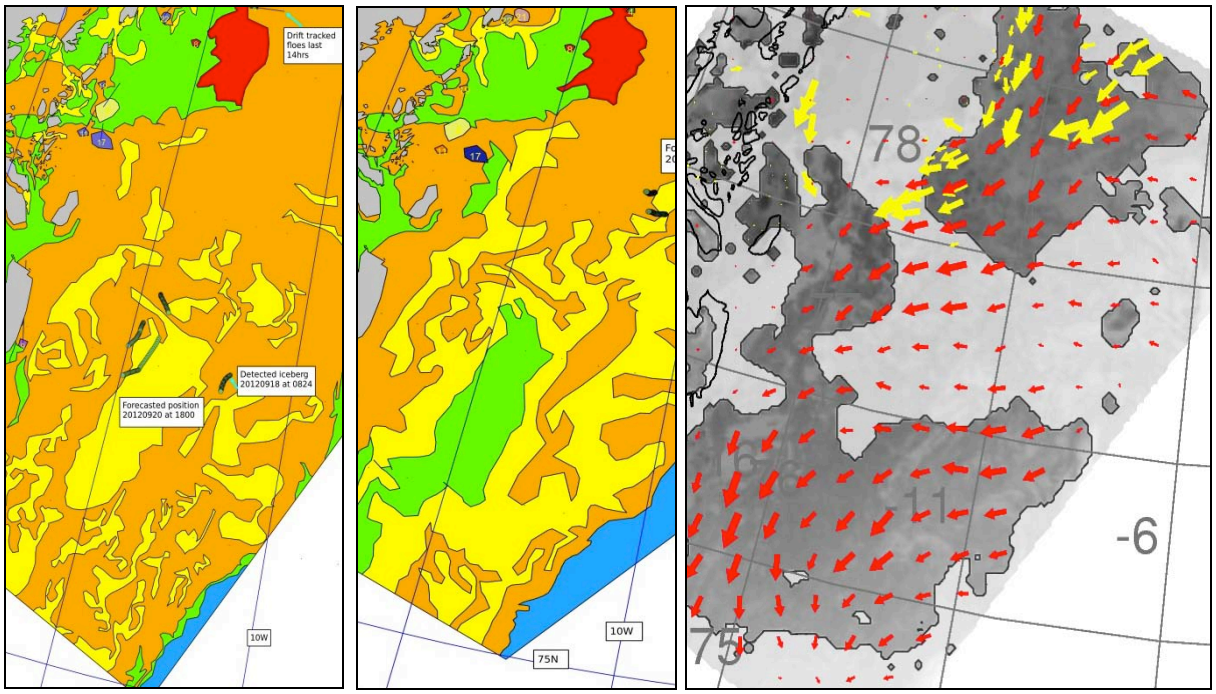

(a) (b) (c)

Figure 4-10: (a) Ice chart from met.no for the 18.09.2012, (b) ice chart from met.no for the 19.09.2012, and (c) ice drift product derived from image pair recorded on 18./19.09.2012

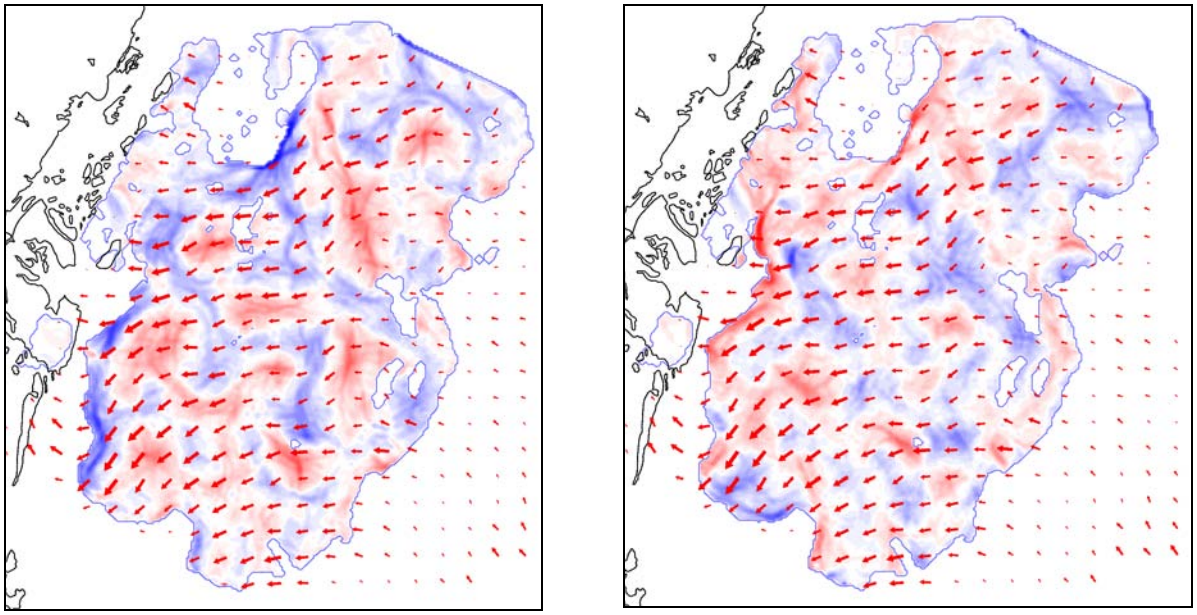

(a) (b)

Figure 4-11: (a) Divergence map derived from Radarsat-2 image pair recorded on 16.09.2012. The red arrows are the calculated velocity field. Red are zones of divergence, blue zones are convergent regions. (b) Vorticity map from the same data set. Red areas rotate in anticlockwise direction, while blue areas rotate clockwise.

4.5 Future work

For the upcoming period of the SIDARUS project, we will focus on the following tasks:

- increase the computational efficiency, especially if backmatching is used in conjunction with Radarsat-2 data
- evaluate the combination of HH and HV channels for Radarsat-2 images
- develop a method to validate the results of the deformation analysis
- handle rotation of ice floes in the motion tracking algorithm

References

Canty, M. J., *Image analysis, Classification and Change Detection in Remote Sensing: With Algorithms for Envi/IDL*, CRC/Taylor & Franics, 348 pp., ISBN: 0-8493-7251-8

Eckstein, A. and Vlachos, P. P., *Digital particle image velocimetry (DPIV) robust phase correlation*, Measurement Science and Technology, 20, 5, 2009, p.15, doi:10.1088/0957-0233/20/5/055401

Fily, M and Rothrock, D. A., *Sea ice tracking by nested correlations*, IEEE Transactions on Geoscience and Remote Sensing, vol. GE-25, no. 5, pp. 570-580, 9 1987.

Foroosh, H. et al., *Extension of Phase Correlation to Subpixel Registration*, IEEE Transactions on Image Processing, 11, 2002, pp. 188-200, doi:10.1109/83.988953

Hollands, T., *Motion tracking of sea ice with SAR satellite data*, PhD Thesis, Bremen University, 2012

Komarov, A. and Barber, D., *Detection of sea ice motion from co- and cross-polarized RADARSAT-2 images*, Geoscience and Remote Sensing Symposium (IGARSS), 2012 IEEE International, 2012, 3277-3280

Kwok, R. et al., *An ice-motion tracking system at the Alaska SAR facility*, IEEE Journal of Oceanic Engineering, vol. 15, no. 1, pp. 44-54, 1, 1990.

Jenkin, M. R. et al., *Techniques for disparity measurement*, CVGIP: Image Understanding, vol. 53, no. 1, pp. 14-30, 1, 1991.

Leppäranta, M., *The Drift of Sea Ice*, ed. by P. Blondel, 2nd ed., Springer – Praxis books in Geophysical Sciences, Springer, Berlin/Heidelberg, 347 pp. ISBN: 978-3-642-04693-4, doi:10.1007/978-3-642-04683-4

Lewis, J. P., *Fast Normalized Cross-Correlation*, in Proceedings of Vision Interface 95, Quebec City, Canada, pp. 120-123

Manduci, R. and Mian, G. A., *Accuracy Analysis ofor Correlation-Based Image Registration Algorithms*, in IEEE International Symposium on Circuits and Systems (ISCAS), IEEE, Chicago, IL, pp. 834-837, doi:10.1109/ISCAS.1993.393852

Pan, B. et al., *Mean intensity gradient: An effective global parameter for quality assessment of the speckle patterns used in digital image correlation*, Optics and Lasers in engineering, vol. 48, no. 4, pp. 469-477, 4 2010.

Pearlstine, L. et al., *Textural discrimination of an invasive plant, schinus terebinthifolius, from low altitude aerial digital imagery*, Photogrammetric Engineering & Remote Sensing, vol. 71, no. 3, pp. 289-298, 3 2005.

Schreer, O., *Stereoanalyse und Bildsynthese*. Springer, 2005.

Shavit, U. et al., *Intensity Capping: a simple method to improve cross-correlation PIV results*, Experiments in Fluids, 2007, 42, 225-240

Thomas, M., *Analysis of Large Magnitude Discontinuous Non-rigid Motion*, PhD Thesis, University of Delaware, 2008

END OF DOCUMENT